Open-pit mining activity and stability area mapping in the Pyhäsalmi Mine using a time series of Sentinel-1 images

Olena Kavats, Dmitriy Khramov and Kateryna Sergieieva*

Foreign Company EOS Ukraine, Dnipro 49055, Ukraine

OK, 0000-0002-0172-7856; DK, 0000-0002-1737-7272; KS, 0000-0001-7345-2209

*Correspondence: ekaterina.sergeeva@eosda.com

Abstract: Synthetic aperture radar (SAR) single look complex (SLC) Sentinel-1 data provide continuous all-weather monitoring of the Earth's surface and detection of texture change areas based on coherence maps. A mining intensity assessment method is proposed in this paper to identify activity and stability areas by calculating the temporal activity index (TAI) – the frequency indicator of surface changes. The TAI value was calculated from a time series of coherence-based normalized differential activity index (NDAI) robust to baseline and temporal decorrelation. The method was applied to monitor the surface conditions of the Pyhäsalmi Mine's (Finland) open pits and waste dumps from May to September 2018–2022, using a time series of Sentinel-1A images acquired in vertical transmit and vertical receive (VV) polarization with a 12-day time step. In each of the observation seasons, TAI maps were generated and areas of activity were identified, mainly on the surface of the waste dumps, at the bottom of the backfill open pit and on the slopes of the old open pit. Activity and stability areas were validated using unmanned aerial vehicle (UAV)-based very high spatial resolution visual orthomosaics and digital surface models (DSMs), which confirmed land cover changes in areas with high TAI values and no changes in stability areas.

One of the important tasks of open-pit mining monitoring is the identification of activity areas and unaffected surfaces of mining sites (Wang *et al.* 2020). Open-pit areas mapping is the basis for the automatic calculation of geometric characteristics of mining sites, dynamic assessment and production rates forecasting, identification of environmental disturbance areas of adjacent territories, etc. GPS sensors can solve the mapping problem, but this requires equipping the entire fleet of vehicles, the use of specialized software and technical staff to support the data collection process (Agamennoni *et al.* 2009). The alternative is the use of aerospace images. The scope of their application for monitoring mining activity includes the generation of three-dimensional digital surface models (DSMs) and digital elevation models (DEMs), vertical displacement maps based on synthetic aperture radar (SAR) data, and indicators of the Earth's surface conditions based on multispectral optical and SAR data, with an accuracy corresponding to the spatial resolution of the input data (Gama *et al.* 2020; Parwata *et al.* 2020; Wei *et al.* 2020; Wu *et al.* 2020; Camalan *et al.* 2022).

Very high spatial resolution (up to a few centimetres) unmanned aerial vehicle (UAV) survey data can be used to produce detailed classification maps and DSMs to track surface changes in open pits and waste dumps (Ren *et al.* 2019). However, they are not always available for a number of reasons. Their disadvantages are their high cost, labour intensity (the need for a team of qualified specialists (pilots, data analysts, etc.)), and the legal aspects and rules for issuing flight permits. Many drones have a short battery lifetime, requiring multiple flights or the use of multiple drones when covering large areas (Fernández-Lozano *et al.* 2018). Dependence on weather conditions complicates the survey planning process and leads to its low frequency of use.

DSMs and DEMs are widely used for modelling, visual analysis of surface conditions of open pits and waste dumps, automated change detection, and generation of datasets for mining disturbance detection (Hu *et al.* 2021; Wang *et al.* 2022). They can be generated using commercial satellite data from WorldView-3 (http://www.maxar.com), Pléiades, SPOT 6/7 (http://www.intelligence-airbusds.com), SuperDove (http://www.planet.com), GRUS–1 (http://www.axelspace.com), EOS SAT–1 (eos.com), etc. Open and free DEMs, such as the Shuttle Radar Topography Mission (SRTM), with a spatial resolution of 30 and 90 m, corresponding to 1 and 3 arcsecond grids, respectively, the ALOS Global Digital Surface Model 'ALOS World 3D 30 m (AW3D30)' version (3.2 and 3.1), the ASTER Global Digital Elevation Model (GDEM) 30 m, and the Copernicus DEM 30 m have insufficient spatial resolutions to track changes in small open pit areas

From: Paavola, M., Kotavaara, O., Bogdanov, K., Knobloch, A., Gusat, D. and Joutsenvaara, J. (eds) *Earth Observations and Proximity Sensing Technologies: Enhancing Safety, Sustainability and Efficiency in Mining Operations*. Geological Society, London, Special Publications, **559**,
https://doi.org/10.1144/gslspecpub2023-216

(Yang *et al.* 2011; Santillan and Makinano-Santillan 2016; Abrams *et al.* 2020; AIRBUS 2020; Takaku *et al.* 2020).

SAR data provide the ability for regular all-weather surface monitoring (Zhang 2021). With the launch of the satellites Sentinel-1A on 25 February 2014 and Sentinel-1B on 25 April 2016, it became possible to regularly monitor horizontal and vertical surface displacements in the C-band, vertical transmit and horizontal receive (VH) and vertical transmit and vertical receive (VV) polarizations using the single look complex (SLC) product (Nam *et al.* 2021; Escayo *et al.* 2022). SAR data are most commonly used to estimate vertical displacements of terrain based on radar interferometry (Escayo *et al.* 2022). For example, the persistent scatterer interferometry (PSI) and Small BAseline Subset (SBAS) algorithm have proven to be reliable tools for detecting and monitoring Earth surface deformations (Devanthéry *et al.* 2016; Tang *et al.* 2020). In particular, PSI processing of Copernicus Sentinel-1 mission data has been implemented in the Stanford Method of Persistent Scatterer (StaMPS) software package of the SentiNel Application Platform (SNAP) (Foumelis *et al.* 2018). If a mine plan is available, vertical displacement maps for mine areas allow identification of surface subsidence above and around underground workings and in their vicinity. In the case of open-pit mines, subsidence maps are used to assess the impact of blasting and to evaluate the amount of rock removed from open pits or accumulated in waste dumps. The contours of subsidence areas or new rockfall boundaries provide information on the location of mining activity areas. In some cases, however, surface mining activities may not be associated with changes in elevation but may result in disturbances to the land cover. Such processes include, for example, changes in the ecological condition of territories due to deforestation or reclamation, violations of slope stability indicators, land cover and hydrological disturbances, changes in the shape, integrity and surface conditions (soil, vegetation, water bodies) of open pits and waste dumps, etc., accompanied by changes in the Earth's surface texture. In addition, short-term drastic changes in land cover cause significant decorrelation and make it difficult to detect vertical displacements (Wang *et al.* 2021; Zhang 2021). Coherence maps generated from SAR data reveal areas of surface texture changes directly or indirectly related to mining activity (Chatterjee *et al.* 2010).

Coherence is the modulus of the complex correlation coefficient between two SLC images, which contains information about the amplitude and phase of the radar signal (Lu *et al.* 2021). If there have been no surface changes in the interval between two acquisition dates, the coherence values will be close to 1. Mining operations change the surface texture, causing coherence to decrease to values close to zero (Kellndorfer *et al.* 2022). Washaya *et al.* (2018) used the coherence change detection (CCD) technique to classify areas of change in order to detect and monitor anthropogenic and natural hazards in urban areas. Surface changes between two monitoring dates are recorded as the percentage increase/decrease in coherence relative to the reference observation date. In the case of open pit surface monitoring, the date of the event (mining activity) may not be known in advance. Therefore, this indicator can be used to estimate the amplitude of change for successive dates in the time series and to identify areas of decreasing coherence as potential areas of mining activity. The Otsu method can be used to detect areas of low coherence associated with mining activities (Otsu 1979; Wang *et al.* 2020). It is assumed that the pixels of open-pit mining sites form a low-value mode on the bimodal coherence histogram, and the application of the Otsu method eliminates the need to set an absolute value of the threshold and to investigate the effect of the threshold on the accuracy of the result. Amani *et al.* (2021) produced maps of average coherence and standard deviation over different observation intervals (months, seasons) to classify wetland types. For example, coherence values are higher in forested wetlands than in open water, and areas with submerged vegetation can be characterized by a high standard deviation of coherence. A similar principle can be used to classify open-pit mining sites, and to detect activity and stability zones and vegetated reclamation areas. Borlaf-Mena *et al.* (2021) used the random forest method to solve the classification problem based on a coherence time series for different values of the temporal baseline. Damaged surface areas can be detected based on coherence distribution percentiles (Olen and Bookhagen 2018). First, 'reliable' zones of potential events (excluding forests and agricultural lands) are identified, for which the standard deviation of coherence over the time series is lower than 0.1. Next, the coherence at the estimated event date is compared to a given percentile of the pre-event coherence distribution. If the coherence is below the percentile, it is assumed that the event has occurred. In the case of detecting areas of mining operations, it is possible to evaluate the coherence distribution over a season and to reveal potential 'activity' areas where coherence is below a given percentile.

A frequency approach can be used to calculate the total coherence changes per season. Manzoni *et al.* (2021) calculated the temporal stability index (TSI) as the relative frequency of cases exceeding a given coherence threshold over a time series of Sentinel-1 images. The TSI was used to assess the stability of dunes in the Egyptian and UAE deserts. The coherence threshold is fixed and does not change

over time series of SAR images. The coherence is assumed to be lower than 0.2 for unstable sites (Manzoni *et al.* 2021). At the same time, the threshold value influences the area of sites classified as stable by TSI.

Moon and Lee (2021) proposed using the normalized differential activity index (NDAI) to estimate surface changes based on coherence. The NDAI overcomes the problem of spatial decorrelation ('baseline decorrelation'), divided into volumetric decorrelation and surface decorrelation, and temporal decorrelation, related to the changes in dielectric and structural properties of the scatterers: rain and snow, natural growth, and leaf fall in the vegetated areas (Wang *et al.* 2021). The NDAI calculation eliminates decorrelation not related to mining and provides an activity indicator that is robust to spatial and temporal decorrelation. Stable pixels – areas with time-averaged coherence values greater than 0.9 and standard deviations less than 0.1 – are pre-selected on each coherence image within the time series (Wang *et al.* 2021). The coherence average and standard deviation thresholds are chosen empirically, and can be 0.8 and 0.2, respectively; their values are the subject of a separate study (Moon and Lee 2021). The NDAI is calculated at each observation date as the normalized difference index between the image-averaged coherence in stable pixels and the coherence in pixels of interest. RGB (red, green, blue) composites of NDAIs averaged over observation periods (e.g. single years of observation) allow detection of areas of mining activity (Wang *et al.* 2021).

The aim of this study is to identify activity and stability areas on the surface of the Pyhäsalmi Mine (Finland) from Sentinel-1 coherence time series by calculating the NDAI and frequency indicator of surface changes. To achieve this goal, a method is proposed in this paper for analysing NDAI time series and calculating the temporal activity index (TAI) – a frequency indicator of NDAI values exceeding a given threshold.

Materials and methods

Study area

The Pyhäsalmi Mine is an underground copper, zinc and pyrite mine located near the town of Pyhäjärvi, Pohjois-Pohjanmaa (Northern Ostrobothnia), Finland (Siikanen *et al.* 2022). The mine is currently in the closure phase and mining operations have been stopped since 1 September 2022. There are two open pits on the mine site. The old open pit of *c.* 0.12 km^2, located in the northwestern part of the mine site, was operated from 1962 to 1975. The backfill open pit of *c.* 0.13 km^2 is located in the southeastern part of the mine site and was used for rock-fill extraction. The waste rock is stored in waste dumps. As of September 2022, there are more than five waste rock dumps adjacent to the open pits, which are constantly changing in size and shape (Fig. 1). Changes in open pits and waste dump surfaces are an indirect indicator of the production process intensity.

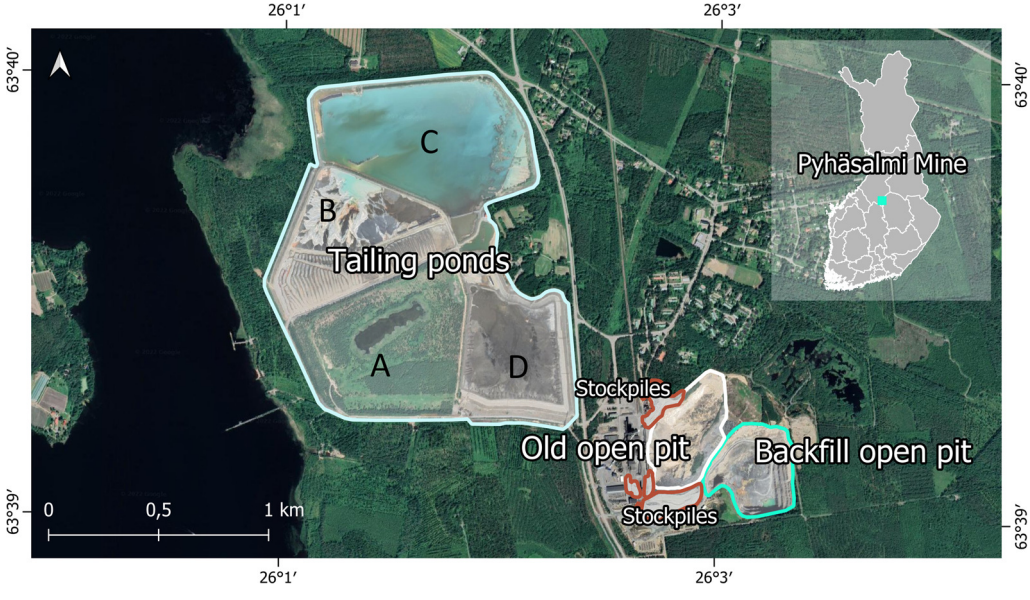

Fig. 1. Study area of the Pyhäsalmi Mine (Finland). Source: basemap, Google Satellite (2024) Pyhäjärvi, available at https://www.google.com/maps (last accessed 18 March 2024).

The observation season in the study area was divided into two periods: from October to April, with snow and ice on the surface, and from May to September, which was a snowless period. Precipitation is frequent throughout the year. There is sparse vegetation on the slopes of the old open pit and forest stands in the areas adjacent to the mine. This affects the coherence values and is a factor of decorrelation, which can cause false activity detection results. Due to the non-flat surface of the mine area and the inclined nature of satellite images, radar shadows can occur on open pits and waste dump slopes.

Remote sensing data

SAR data

Satellite SAR Sentinel-1A SLC images in the interferometric wide (IW) mode were used to detect open-pit mining activity and stability areas. The Pyhäsalmi Mine area is covered by six Sentinel-1A paths: 14, 87 and 160 (ascending), and 51, 80 and 153 (descending). The path 153 data were used in this study. The path 153 image parameters are flight direction descending, frames 378 and 379.

Coherence time series from May to September 2018–2022 were generated using Sentinel-1A SLC IW data. The ability to observe surface conditions at the Pyhäsalmi Mine depends on the season. According to the Finnish Meteorological Institute (ilmatieteenlaitos.fi), the snow season in Finland generally lasts from November to March. The period from May to September was chosen because of the absence of snow and ice on the ground surface, the presence of which can cause a decrease in coherence and errors in the results. The time interval between the acquisitions was 12 days. Sentinel-1B data from 2018 to 2021 were not used in this study because the spacecraft was subject to an anomaly on 23 December 2021, resulting in a loss of data transmission (Potin *et al.* 2022). As ground verification data are only available for 2022, Sentinel-1B data were also excluded from previous years' observations to maintain the integrity of the experiment. The total number of Sentinel-1A images for the entire observation period was 60. The total number of coherence maps was 54 (Fig. 2). Data were provided by the Golden-AI platform (http://www.goldeneye-project.eu/ai-platform) and the ASF Data Search Vertex service (search.asf.alaska.edu) (Havisto *et al.* 2021). Data in VV polarization were used in this study (Wang *et al.* 2021)

Sentinel-1A SLC data were preprocessed according to the following main stages (Fig. 3) (Kavats *et al.* 2020; Kellndorfer *et al.* 2022):

(1) applying orbit information about satellite position during the SAR data acquisition;
(2) back geocoding: co-registration of two split products based on the orbit information added in the previous step and information from a DEM;
(3) coherence estimation: coherence was calculated as a separate raster band and showed how similar each pixel was between the slave and master images on a scale from 0 to 1;
(4) TOPSAR deburst: removing the seam lines between the single bursts;
(5) multilook: speckle reduction to eliminate random outliers;
(6) range Doppler terrain correction: geocodes the image by correcting SAR geometric distortions using a DEM and produces a map-projected product.

The enhanced spectral diversity (ESD) method estimates constant azimuth offset of SAR images and minimizes the inhomogeneity of bursts, allowing the interferogram fragments to be combined (Wang *et al.* 2017). Since the study area is located within a single burst, this method was not used.

The Pyhäsalmi Mine area is located at 63.66° north latitude; therefore, SRTM 1 arcsecond DEM

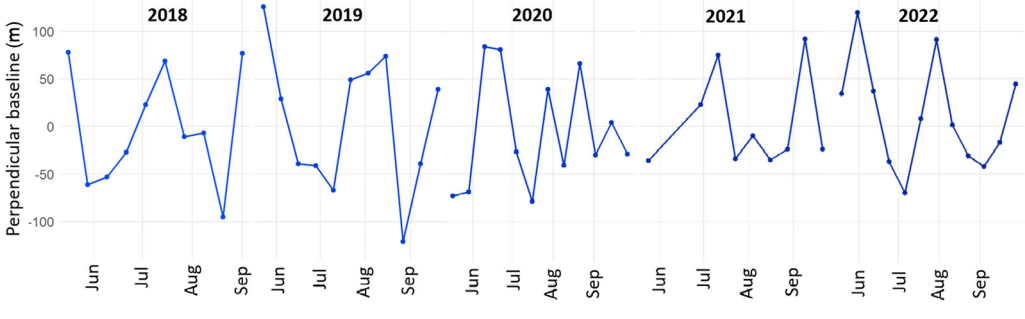

Fig. 2. Dates of Sentinel-1A coherence maps from orbit 153 and perpendicular baseline values for the 12-day time interval.

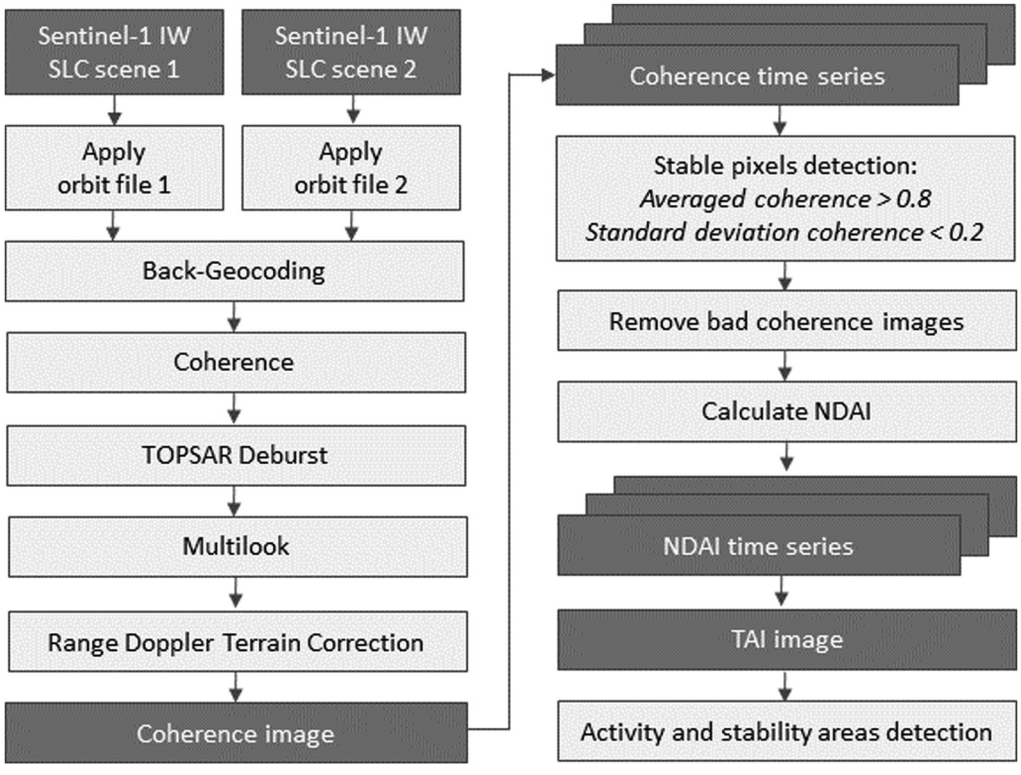

Fig. 3. General workflow diagram describing the main steps of the activity and stability areas detection method by coherence, normalized differential activity index (NDAI) and temporal activity index (TAI) calculation.

data could not be used for the ellipsoidal Earth phase and topographic phase removal (its data is limited to latitudes between –60° and 60°). Instead, the Copernicus GLO-30 DEM was used (COP-DEM 2019; AIRBUS 2020).

Ancillary data

Visual orthomosaics and DSMs of open pits and waste dumps at spatial resolutions of 0.019 and 0.038 m, respectively, were used to verify the activity and stability area detection results. Areas of surface elevation change associated with mining operations were identified using DSM data. Data were provided by Sitemark (http://www.sitemark.com) based on UAV surveys on 6 June 2022 and 6 September 2022

In addition, the *in situ* data on soil conditions, mine surface vegetation and the location of mine workings were collected on 30 August and 1 September 2022. Figure 4 shows images of the backfill open pit and pyrite concentrate dump.

There are numerous small groundwater outflow areas at the bottom of the backfill open pit, which may influence the spatial distribution of coherence and reduce its values. The waste dump surfaces are homogeneous and there is no vegetation on the slopes.

Mining activity detection method

A method for detection activity and stability areas on the mine surface is proposed in this paper. The method is based on the analysis of NDAI time series generated from Sentinel-1 coherence maps and calculation of the frequency indicator of NDAI variations relative to a given threshold within the observation season (Sergieieva *et al.* 2023).

Coherence calculation

Coherence is estimated as a complex correlation coefficient between two SLC images. It describes the closeness of correlation between the complex pixel values of two SLC images s_{t_1} and s_{t_2} at consecutive acquisition dates t_1 and t_2, and is calculated in a sliding window of size $N \times M$ pixels (Jacob *et al.*

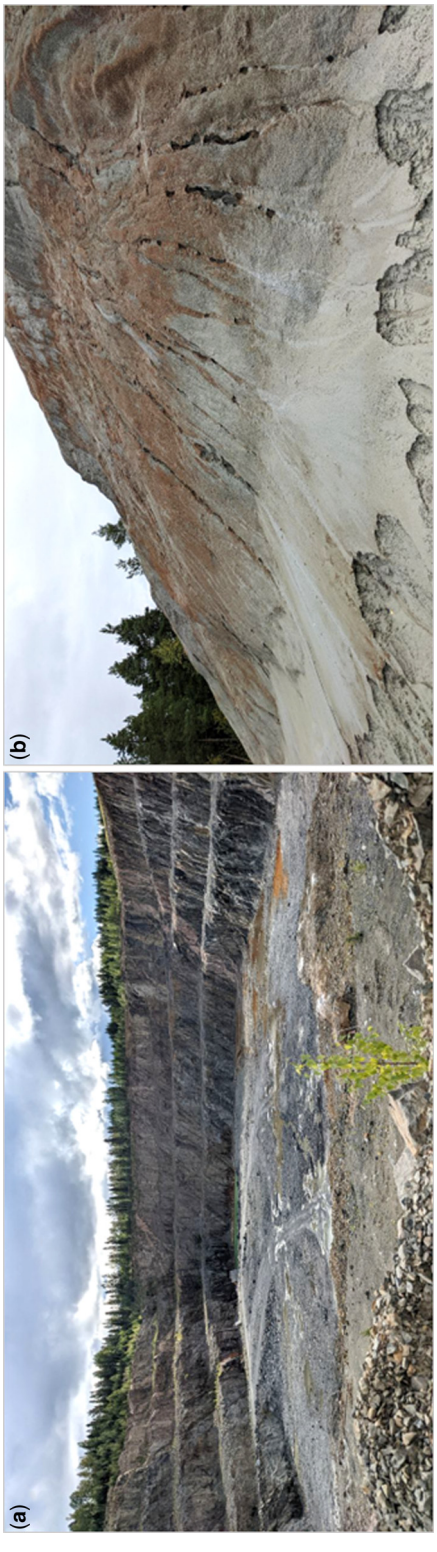

Fig. 4. Ground observations of the Pyhäsalmi Mine surface conditions on 30 August 2022: (**a**) backfill open pit; (**b**) slope of the pyrite concentrate dump in the northern part of the mine site.

2020; Wang *et al.* 2021; Villarroya-Carpio *et al.* 2022):

$$\gamma = \frac{\left|\sum_{i=1}^{N}\sum_{j=1}^{M} s_{t_1}(x_i,y_j) \times s_{t_2}^{*}(x_i,y_j)\right|}{\sqrt{\sum_{i=1}^{N}\sum_{j=1}^{M} |s_{t_1}(x_i,y_j)|^2 \times \sum_{i=1}^{N}\sum_{j=1}^{M} |s_{t_2}(x_i,y_j)|^2}} \quad (1)$$

where x_i, y_j, $i = 1, \ldots N$, $j = 1, \ldots M$ are the spatial coordinates of image pixels and * represents complex conjugation.

A sliding window of size 10 × 3 in range and azimuth was used in this paper (Moon and Lee 2021). The spatial resolution of the resulting image was 20 m.

Coherence values range from 0 to 1, where 0 means absolute decorrelation and 1 is the maximum similarity (Wang *et al.* 2021). Stable surface areas are characterized by coherence values close to 1 (Moon and Lee 2021). To identify stable pixels with high coherence values throughout the time series, Moon and Lee (2021) proposed to calculate the temporal mean and standard deviation of the coherence in each pixel (Fig. 5a, b). In stable pixels, the temporal average of coherence is higher than 0.8 and the temporal standard deviation of coherence is lower than 0.2 (Fig. 5c).

Calculation of NDAI

Coherence decrease due to phase decorrelation is caused by the influence of various factors. There are thermal, spatial and temporal decorrelations. The influence of thermal noise is typically neglected due to the good signal-to-noise ratio of modern SAR sensors (Lee and Liu 2001; Funning and Garcia 2019; Wang *et al.* 2021). Spatial ($\gamma_{spatial}$) or baseline decorrelation consists of volume (γ_{volume}) and surface ($\gamma_{surface}$) decorrelation (Lu *et al.* 2018; Wang *et al.* 2021). Volume decorrelation is generally observed in areas of vegetation cover. For example, at the Pyhäsalmi Mine site, sparse vegetation covers the slopes of the old open pit and the areas adjacent to the mine sites have dense forest cover. Surface decorrelation is caused by the terrain and depends on the perpendicular baseline ($\gamma_{baseline}$). As the perpendicular baseline increases, coherence decreases (and surface decorrelation increases). A decrease in coherence in the interval between two surveys, or temporal decorrelation ($\gamma_{temporal}$), is associated with changes in dielectric properties and the Earth's surface texture due to meteorological events ($\gamma_{weather}$), changes in vegetation conditions, mining operations ($\gamma_{activity}$) and other factors (Zhang *et al.* 2020; Moon and Lee 2021; Villarroya-Carpio *et al.* 2022). Temporal decorrelation can be caused by changes in the vegetation leaf area (leaf emergence in spring and

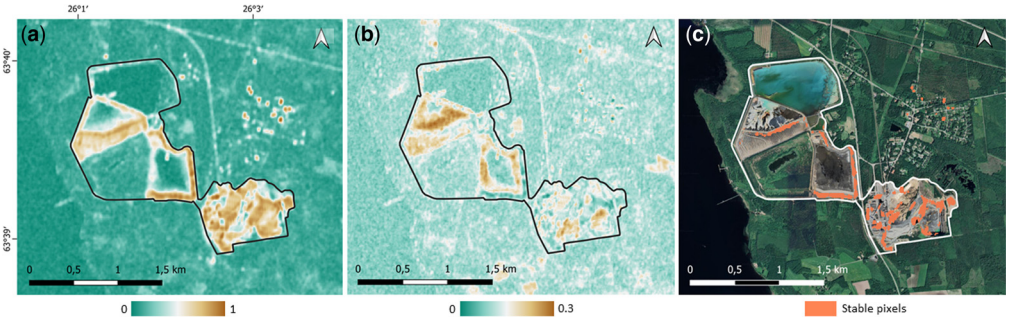

Fig. 5. Preliminary analysis of the Sentinel-1A coherence time series for 2018–2022: (**a**) temporal average of coherence; (**b**) standard deviation of coherence; (**c**) stable pixels for which the temporal average of coherence is higher than 0.8 and the temporal standard deviation of coherence is lower than 0.2. Source: basemap, Google Satellite (2024) Pyhäjärvi, available at https://www.google.com/maps (last accessed 18 March 2024).

leaf fall in autumn), precipitation (snow, rain) and surface works. From October to May there is snow on the surface of the Pyhäsalmi Mine, weather conditions are unstable and precipitation is very frequent. This period was therefore excluded from the analysis.

Decorrelation can be represented as follows (Moon and Lee 2021; Wang *et al.* 2021):

$$\gamma = \gamma_{\text{spatial}} \times \gamma_{\text{temporal}} = \gamma_{\text{baseline}} \times \gamma_{\text{weather}} \times \gamma_{\text{activity}}. \quad (2)$$

Wang *et al.* (2021) proposed excluding the influence of weather conditions on the coherence reduction by calculating the spatial average γ^{stable} in stable pixels for each coherence image. In some cases, the spatial average in γ^{stable} was lower than 0.8 (Fig. 6a), which can be caused by weather conditions. In early May, the air temperature reached positive values and snow and ice melted. On other days, the Landsat 8 and Sentinel-2 optical images often had a high cloud cover rate. Sentinel-1 images with average spatial coherence lower than 0.8 were excluded from further processing. Thus, the resulting coherence time series consisted of 43 images and decorrelation can be represented as:

$$\gamma = \gamma_{\text{spatial}} \times \gamma_{\text{temporal}} = \gamma_{\text{baseline}} \times \gamma_{\text{activity}}. \quad (3)$$

The influence of the perpendicular baseline value on the coherence variation was evaluated. For the Sentinel-1A SLC image sample, the absolute values of the perpendicular baseline, after excluding images with coherence lower than 0.8, ranged from 1 to 121 m. Figure 6b shows a linear regression of the spatially averaged coherence values in stable pixels on the perpendicular baseline. There was a downward trend: coherence decreased slightly with the increase in the perpendicular baseline. The Pearson

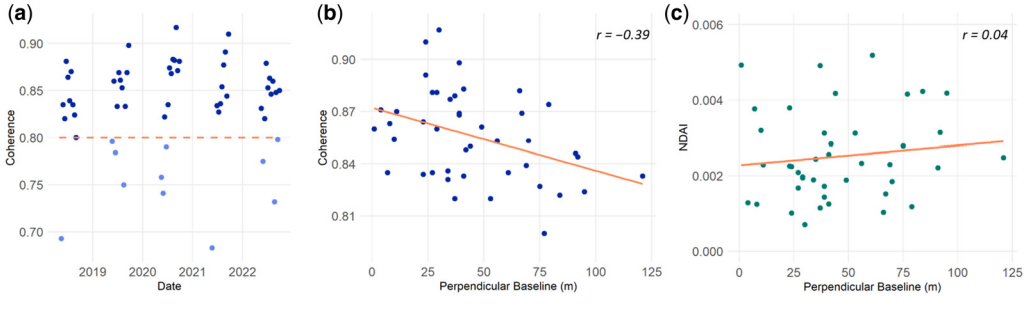

Fig. 6. Scatterplots of Sentinel-1A spatially averaged coherence in stable pixels for different acquisition dates and perpendicular baseline values, 2018–2022: (**a**) average coherence in stable pixels on each acquisition date (images with spatially averaged coherence in stable pixels lower than 0.8 were excluded from further analysis); (**b**) linear regression of the average coherence in stable pixels on the absolute value of the perpendicular baseline; (**c**) linear regression of spatially averaged normalized differential activity index (NDAI) in stable pixels on the absolute value of the perpendicular baseline.

correlation coefficient was −0.39 and the *P*-value was 0.01 (less than 0.05), indicating that the correlation was statistically significant. For comparison, in the paper by Wang *et al.* (2021), the Pearson's pairwise correlation coefficient was −0.33 for a sample of 70 observations, with a *P*-value equal to 0.005.

It can be seen that γ_{baseline} still affected the coherence and prevented its use as a measure of the change in surface decorrelation due to mining activity. To reduce γ_{baseline}, Moon and Lee (2021) proposed the calculation of the NDAI to reduce decorrelation using the spatial average of γ^{stable} coherence in stable pixels:

$$\text{NDAI} = \frac{\gamma^{\text{stable}} - \gamma^{\text{target}}}{\gamma^{\text{stable}} + \gamma^{\text{target}}} \tag{4}$$

where γ^{stable} is the spatial average of coherence in stable pixels and γ^{target} is the coherence value in each target pixel of each coherence image.

Taking into account the components of the decorrelation, the NDAI can be represented as follows (Wang *et al.* 2021):

$$\text{NDAI} = \frac{\gamma^{\text{stable}}_{\text{baseline}} \times \gamma^{\text{stable}}_{\text{activity}} - \gamma^{\text{target}}_{\text{baseline}} \times \gamma^{\text{target}}_{\text{activity}}}{\gamma^{\text{stable}}_{\text{baseline}} \times \gamma^{\text{stable}}_{\text{activity}} + \gamma^{\text{target}}_{\text{baseline}} \times \gamma^{\text{target}}_{\text{activity}}}. \tag{5}$$

Since the spatial decorrelation γ_{baseline} is approximately the same in stable and target pixels for each coherence map ($\gamma^{\text{stable}}_{\text{baseline}} = \gamma^{\text{target}}_{\text{baseline}}$), the NDAI equation can be represented as follows (Wang *et al.* 2021):

$$\text{NDAI} = \frac{\gamma^{\text{stable}}_{\text{activity}} - \gamma^{\text{target}}_{\text{activity}}}{\gamma^{\text{stable}}_{\text{activity}} + \gamma^{\text{target}}_{\text{activity}}}. \tag{6}$$

The NDAI values are mostly in the range from 0 to 1. NDAI values close to 0 correspond to the most stable areas, while values close to 1 correspond to activity areas. If the coherence in a pixel is higher than γ^{stable}, the NDAI values are negative.

Calculation of the TAI

Mining processes disturb the integrity of the Earth's surface and change its texture. The TAI is an estimate of mining intensity and is calculated as the relative frequency of dates with low coherence and high NDAI values (Manzoni *et al.* 2021). The TAI is designed to identify areas of intense mining, as well as stable areas where the surface texture has changed little. The NDAI was used as an estimate of mining activity, where high values correspond to a high intensity of change. th_{NDAI} is the NDAI threshold value. At each date of coherence calculation t on a time series of T observations ($t = 1, \ldots, T$), a binary raster mask of activity and stability areas was created. The pixels of the mask were equal to 1 if $\text{NDAI}_t > \text{th}_{\text{NDAI}}$ and 0 in the opposite case.

$$\text{TAI} = \frac{1}{T}\sum_{t=1}^{T}(\text{NDAI}_t > \text{th}_{\text{NDAI}}). \tag{7}$$

To determine the th_{NDAI} value more precisely, the Otsu method of finding a local minimum on the bimodal histogram was used, according to the following steps (Wang *et al.* 2020; Kavats *et al.* 2022):

(1) remove NDAI outliers (NDAI values below the 0.005 quantile or above the 0.995 quantile were replaced by the corresponding quantile);
(2) evaluate the distribution density function (kernel density estimation with a Gaussian kernel);
(3) find the local minimum of the distribution density function;
(4) check whether the minimum is close to one of the histogram edges – if not, the required threshold has been found.

Each pixel of the TAI map contained the frequency of observation dates with low coherence and high NDAI values, which was a statistical estimate of the probability of mining operations. The time series of TAI maps generated for each observation season allowed tracking of the dynamics of mining operations and monitoring of changes over time.

The general workflow of the activity and stability areas detection method is shown in Figure 3.

Calculation steps were implemented in the R programming language of version 4.1.1 (R Core Team 2020) in the Integrated Development Environment (IDE) RStudio 2021.09.0 (RStudio Team 2022), using the 'terra' package (Hijmans 2022).

Results

NDAI maps

Figure 7 shows typical examples of coherence and NDAI maps for some monitoring dates for 2019 and 2022, as well as the closest date-matched high-spatial-resolution optical images from the Google Earth service. The top line (Fig. 7a–c) shows the 2019 data, including SAR data for 3 August 2019 and the optical image for 28 July 2019. The bottom line (Fig. 7d–f) shows the 2022 data, including SAR data for 4 September 2022 and the optical image for 29 July 2022.

The most stable sites with high coherence (Fig. 7a, d) and low NDAI values (Fig. 7b, c) were mainly located in the open-pit areas of the Pyhäsalmi

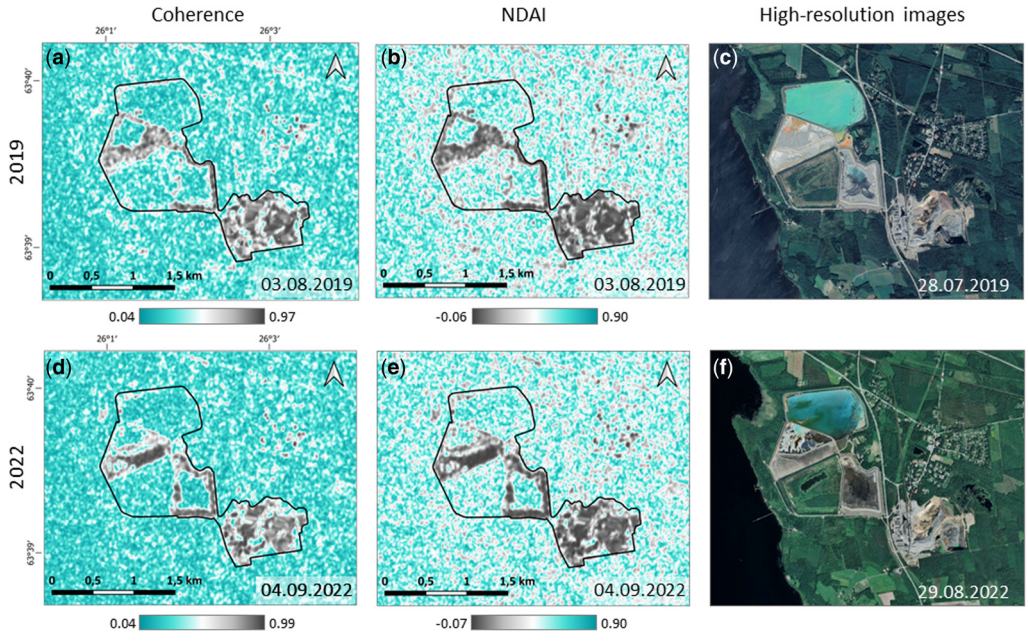

Fig. 7. Comparison of coherence maps, the normalized differential activity index (NDAI) and the closest date-matched high spatial resolution optical satellite images for some 2019 (a–c) and 2022 (d–f) dates. (**a**) Sentinel-1 coherence on 22 July 2019–03 August 2019; (**b**) Sentinel-1 NDAI on 22 July 2019–03 August 2019; (**c**) Google Earth high spatial resolution image from 28 July 2019; (**d**) Sentinel-1 coherence on 23 August 2022–04 September 2022; (**e**) Sentinel-1 NDAI on 23 August 2022–04 September 2022; (**f**) Google Earth high spatial resolution image from 29 August 2022.

Mine and near the tailing ponds. Some high coherence values were observed along the roads. The rest of the area was covered by water bodies, including Lake Pyhäjärvi and active tailings ponds, and forest and agricultural lands, the surface texture of which is constantly changing, resulting in low coherence (high NDAI) values.

The maps in Figure 7a, d show the actual range of coherence values, which can be extended to minimum and maximum acceptable values from 0 to 1 for the purpose of comparing multi-temporal maps. As the spatial average of coherence in stable pixels for each individual monitoring date was used to calculate the NDAI, there was no single standard range of NDAI values, making it difficult to quantitatively and visually compare multi-temporal NDAI maps. The range of NDAI values was slightly larger than the range of coherence values (up to 0.08) and in some cases did not significantly exceed 1 (up to 1.04). For the time series analysed, NDAI values generally ranged from −0.10 to 0.95, and coherence values ranged from 0.02 to 0.99.

Figure 8 shows the relationship between the pixel values of the coherence and NDAI maps, their histograms for 4 September 2022 (Fig. 7d, e) and the averaged data for 2018–2022.

As shown in Figure 8a, the NDAI and coherence values were characterized by a non-linear (hyperbolic) relationship: a narrow range of low coherence values corresponded to a wider range of high NDAI values and vice versa. For example, low coherence values from 0.04 to 0.25 (range 0.21) corresponded to NDAI values from 0.54 to 0.91 (range 0.37), and high coherence values from 0.50 to 0.99 (range 0.49) corresponded to NDAI values from −0.08 to 0.26 (range 0.34). This should be taken into account when selecting thresholds to distinguish areas of activity from areas of stability. As a result of the non-linearity of the relationship, the NDAI histogram for the data from 4 September 2022 had a more pronounced narrow mode of low values corresponding to high coherence values (Fig. 8b, c). For the 2018–2022 averaged images, the histograms had narrow modes of high NDAI and low coherence values corresponding to areas of continuous surface texture change, and a wide 'plateau' of high coherence values and low NDAI values corresponding to stable areas of the Earth's surface (Fig. 8d, e).

The minimum and maximum values of the NDAI averaged for the time series of 43 images for 2018–2022 were −0.05 and 0.64, respectively. For the averaged coherence, the minimum and maximum

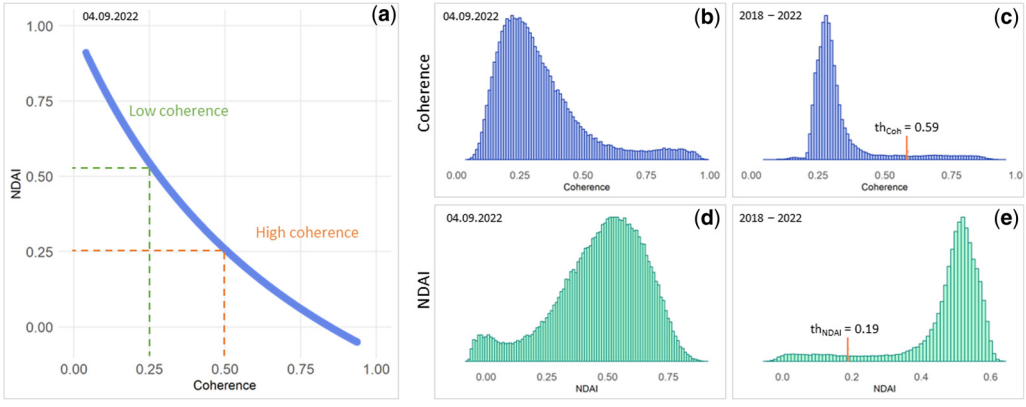

Fig. 8. Relationship between coherence and normalized differential activity index (NDAI) values for Sentinel-1 data on 4 September 2022. (**a**) Functional relationship; (**b**) histogram of coherence values on 4 September 2022 (Fig. 7d); (**c**) histogram of averaged coherence values for 2018–2022; (**d**) histogram of NDAI values on 4 September 2022 (Fig. 7e); (**e**) histogram of averaged NDAI values for 2018–2022.

values were 0.05 and 0.95, respectively. The threshold values for NDAI th_{NDAI} and coherence th_{Coh} indicated separate activity and stability areas. Wang *et al.* (2021) suggested using 0.2 as the threshold value, which roughly corresponded to the middle of the 'plateau' of low values in the histogram of the averaged NDAI (Fig. 8e).

The threshold obtained for the averaged NDAI data $th_{NDAI} = 0.19$ was close to the one proposed by Wang *et al.* (2021) (Fig. 8e). $th_{Coh} = 0.59$ (Fig. 8c). NDAI values higher than th_{NDAI} (coherence values lower than th_{NDAI}) corresponded to areas of activity. In comparison, Manzoni *et al.* (2021) proposed detecting activity areas using a coherence threshold of 0.2. The obtained threshold th_{NDAI} was used to separate activity and stability areas based on the TAI.

TAI maps

Figure 9 shows NDAI and TAI maps averaged over a time series of 43 observations (2018–2022). The least stable areas were the water surfaces of Lake Pyhäjärvi and the Pyhäsalmi Mine tailing ponds, as well as forest and agricultural vegetation around the mine. For these areas, the average NDAI values were close to 0 or negative (Fig. 9a), and the TAI values were close to 1. The most stable areas are the open artificial surfaces (asphalt pads, roofs of buildings and facilities) in the Ruotanen settlement, located 0.5 km north of the mine. The TAI values were close to 0.5 and higher for roads to the NE of the mine, which may have been due to the influence of adjacent vegetation cover and mixed pixels which falsely intensified the activity indicators.

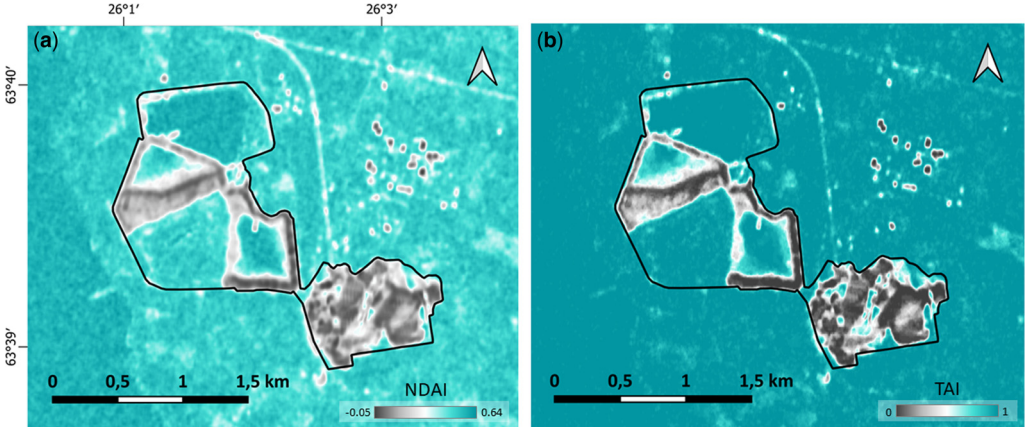

Fig. 9. Averaged maps for 2018–2022. (**a**) Normalized differential activity index (NDAI); (**b**) temporal activity index (TAI).

The mine's tailing ponds contained areas of activity and stability. Tailing pond A (Fig. 1) was decommissioned in October 1997 (Kavats *et al.* 2022). Its surface is covered by sparse vegetation with a constantly changing surface texture, and it was characterized by low NDAI and high TAI values. Tailing ponds B and D are active and contain pyrite concentrate (Mäkinen and Lerssi 2007). The southern part of tailing pond B is a relatively stable area of open ground with low-intensity alteration. The central part of the pond contains a mixture of industrial wastewater. The dam surface in the western and northeastern parts of the ponds is also relatively stable over time. Tailing pond D is actively operated and the unvegetated slopes of its northern and eastern dams are almost unchanged over time. Tailing pond C is a sump and functions as a mine water basin (Kavats *et al.* 2022). The persistent presence of water causes continuous changes in surface texture, resulting in low NDAI and high TAI values.

Open-pit mining, waste dump formation and processing occur with varying intensities in different areas. High and close to 0.5 TAI values (Fig. 9b) were mainly observed in the backfill open pit, in the areas of waste dumps to the east of the old open pit and on the vegetated eastern slope of the old open pit. The mine area mainly consists of open surfaces with low intensity of change.

It should be noted that TAI characterizes the intensity of changes in surface texture (horizontal component of mining operations) and does not represent information on changes in waste dump height and open-pit depth (vertical component).

Figure 10f–j shows TAI maps for each year of observation. For comparison, Figure 10a–e shows the Sentinel-2 RGB composites for one of the dates of each year. Contours of open pits and waste dumps are shown in white (Fig. 1).

High TAI values along the study area boundaries were primarily caused by forest stands forming mixed pixels. Sparse vegetation is present on the eastern slope of the old open pit, where areas of increased activity associated with permanent changes in canopy texture were observed in all years. High TAI values were observed on the western slope of the backfill open pit. This may have been caused by the inclined descending orbit of a satellite moving from north to south (Kavats *et al.* 2022). Uneven terrain caused radar shadows on the open-pit slopes, which looked like areas of low coherence and could be misinterpreted as activity zones. This assumption needs to be verified by comparing activity maps from two orbits (ascending and descending) and will be the subject of further research.

Based on the TAI time series analysis (Fig. 10f–j), the following conclusions can be drawn. During the observation period, the area of activity at the bottom of the backfill open pit moved from its southwestern to its northeastern part. The intensity of the activity varied and reached its maximum in 2020 and 2021. The waste dump in the northern part of the mine has changed in shape and area. Continuous intense changes were observed in the central part of the old open pit. Some activity was observed on the adjacent eastern slope, probably caused by crumbling of waste rock or slope instability. Continuous changes related to mining activities were observed on the surface of the waste dump in the southern part of the study area and on the adjacent southern slope of the old open pit. In 2018, the intensity of changes reached their maximum in the western part of waste dump, in 2020 it was more pronounced in the eastern part, and in 2021 and 2022 the maximum changes were observed in the northern part. Changes in the open-pit slope texture may also have been related to rock crumbling. At administrative buildings and industrial facilities locations, waste rock is periodically dumped and removed, resulting in small activity indicators. In general, the northern part of the backfill open pit, northern and eastern slopes of the old open pit, and open surfaces in the western part of the study area remained the most stable (TAI values close to zero) during the observation period.

Figure 10k–p shows the areas where changes occurred on half or more of the observation dates of each monitoring period (activity areas, $TAI \geq 0.5$) or where there were no changes (stability areas, $TAI = 0$). When identifying activity and stability areas (Fig. 10k–o) based on TAI maps (Fig. 10f–j), vegetation, radar shadows and water surfaces were preliminarily eliminated.

During the observation period from 2018 to 2022, production-related surface changes at the Pyhäsalmi Mine occurred mainly in the eastern and northern parts of the backfill open pit, on the northern slope of the nearest waste dump, on the slopes of the waste dump in the northern part of the mine, and in areas near administrative buildings and facilities. In 2022, the mining activity areas identified by the TAI map were verified by UAV RGB visual orthomosaics and DSM data: TAI values higher than zero corresponded to the largest vertical changes on the Earth's surface. The most stable areas were in the northern and southern parts of the backfill open pit, on the old open-pit slopes, and in the western and southern parts of the mine area.

Mining activity analysis

Outlining zones of interest

Consider some areas with TAI values above zero (activity zones) and mine surface fragments with

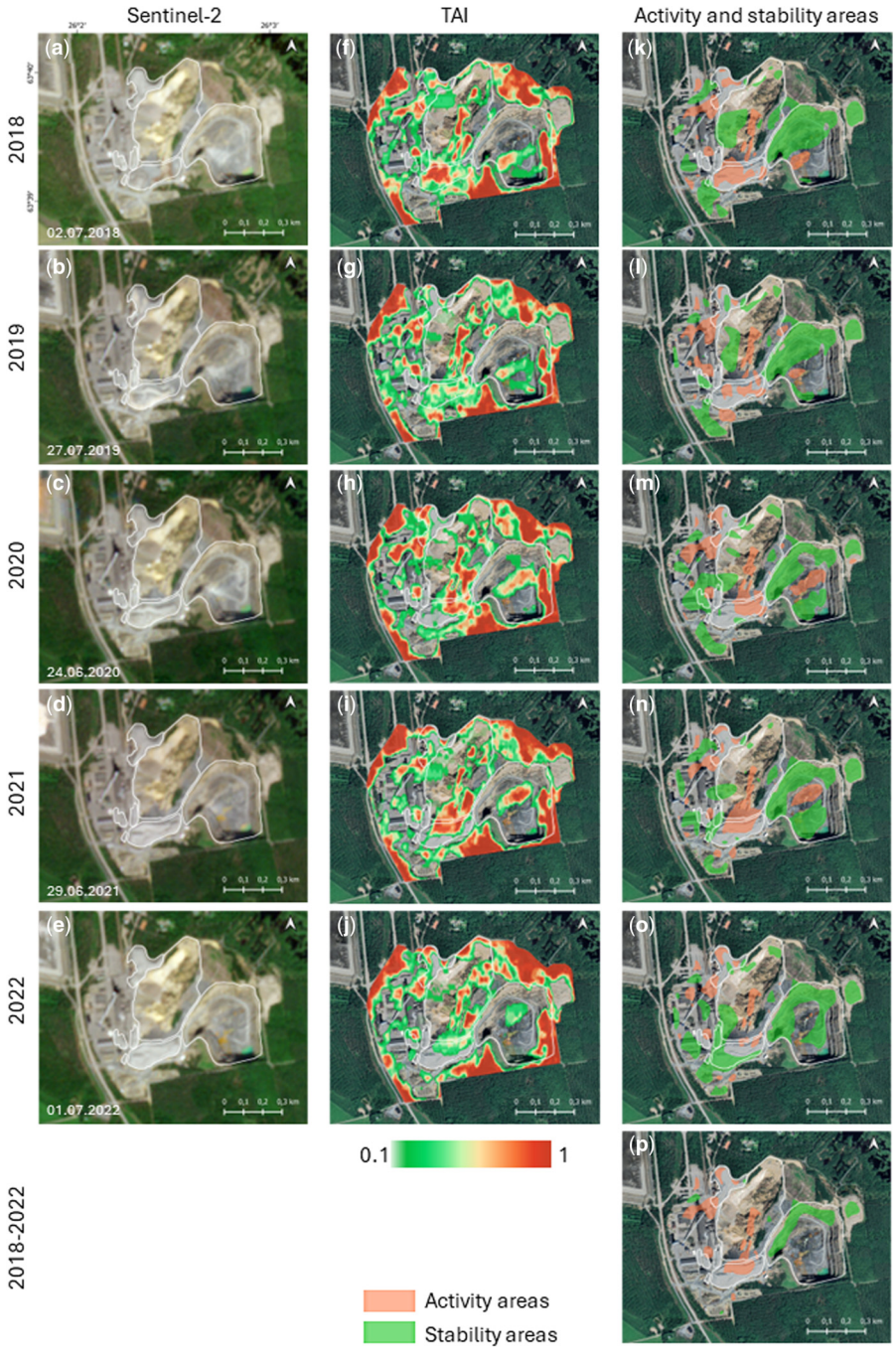

Fig. 10. (a–e) Sentinel-2 RGB composites (column 'Sentinel-2'): (**a**) on 2 July 2018; (**b**) on 27 July 2019; (**c**) on 24 June 2020; (**d**) on 29 June 2021; (**e**) on 1 July 2022. (f–j) Temporal activity index (TAI) maps generated from May to September of each monitoring year (column 'TAI'): (**f**) 2018; (**g**) 2019; (**h**) 2020; (**i**) 2021; (**j**) 2022. (k–p) Contours of activity areas (TAI $\geq$ 0.5) and stability areas (TAI = 0) at open pits and waste dumps excluding vegetation, radar shadows and water surfaces in each of the monitoring years (column 'Activity and stability areas'): (**k**) 2018; (**l**) 2019; (**m**) 2020; (**n**) 2021; (**o**) 2022; (**p**) 2018–2022. Source: basemap, Google Satellite (2024) Pyhäjärvi, available at https://www.google.com/maps (last accessed 18 March 2024).

zero TAI (stability zones). There are several zones of interest (Fig. 11):

(1) activity zone 1 (A1): pyrite concentrate in the northern part of the mine site;
(2) activity zone 2 (A2): waste dumps near administrative buildings and facilities;
(3) activity zone 3 (A3): waste dumps in the southern part of the mine site and the southern slope of the old open pit;
(4) stability zone 1 (S1): open surface area in the northern part of the old open pit;
(5) stability zone 2 (S2): northwestern slope of the backfill open pit;
(6) stability zone 3 (S3): open surface area in the eastern part of the mine site.

Waste dump surfaces in active areas are subject to continuous changes due to production processes. As part of the Goldeneye project, interferometric SAR (InSAR)-based measurements of displacements performed by Callio Lab Research Centre using Sentinel-1 data for June–September 2022 showed modified surface slope erosion on waste dump surfaces in zones A1 and A3, which was another factor of surface change (Kotavaara *et al.* 2023). In different years, TAI values different from 0 and/or close to 1 (Fig. 10) have been observed in different parts of zones A1–A3, only rarely covering the whole area of each zone. In stability zones, activity is either completely absent or present in small fragments of each site, but TAI values in these zones are close to zero.

To confirm the presence of mining activities in zones A1–A3, it was checked whether vertical displacements of the Earth's surface occurred there. To do this, DSM data were used for June and September 2022.

Comparison of TAI maps with DSM maps

In 2021–2022, as part of the Goldeneye project, field trials were conducted at the mine site, including UAV data collection. The Sitemark company surveyed a 1.51 km^2 area, employing a pilot with a

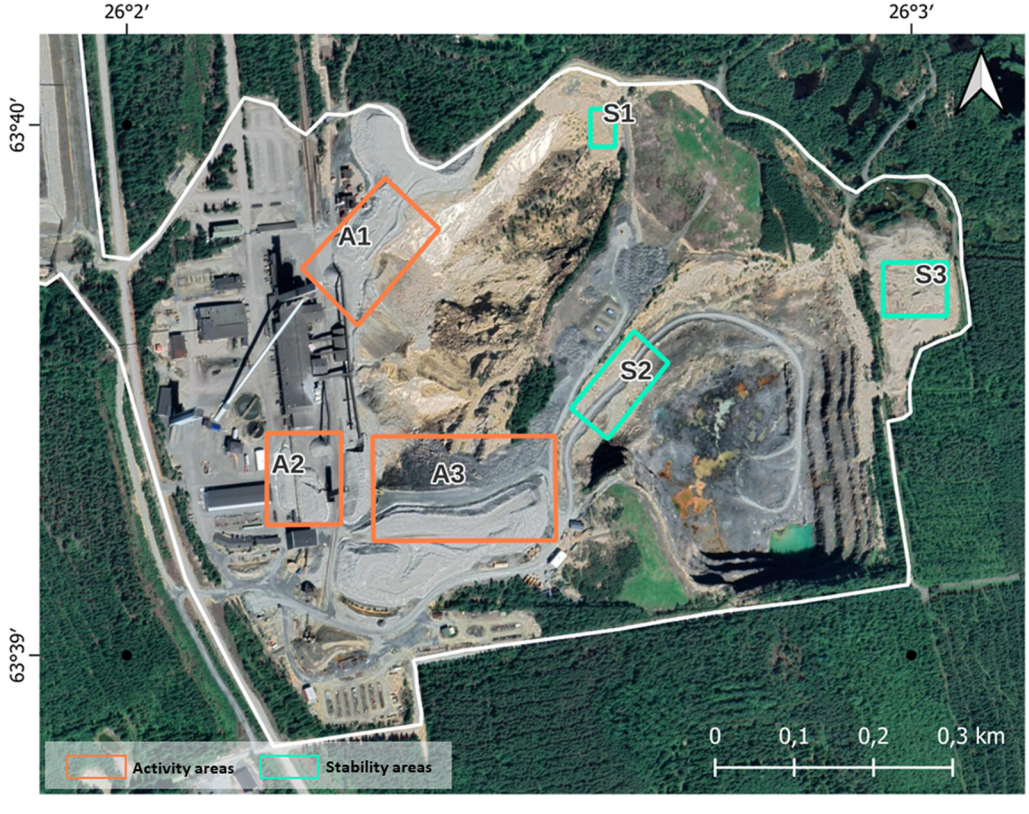

Fig. 11. Selected activity (A) and stability (S) zones in the Pyhäsalmi Mine area for 2018–2022. Source: basemap, Google Satellite (2024) Pyhäjärvi, available at https://www.google.com/maps (last accessed 18 March 2024).

DJI Matrice 300 RTK and DJI Zenmuse P1 sensor. The survey was carried out on 9 September 2021, 6 June 2022 and 6 September 2022. The first survey date was excluded from consideration as the identification of surface changes between September 2021 and June 2022 required consideration of the periods with snow and ice (from mid-autumn to mid-spring). Data from the second and third surveys were used to analyse and validate the results. On each of the dates, Sitemark provided DSMs from drone-operated RGB sensing.

To identify vertical surface displacements between the second and third surveys, the DSM difference was calculated (Fig. 12a). The mean height difference for the study area is 0.4 m and the standard deviation is 1.2 m. Figure 12a shows the height differences in the range of mean $\pm$ standard deviation, but there are variations outside this range. They are represented in Figure 13a by the colours of the difference limit values.

A TAI map was generated using six NDAI maps in the date range from 24 June to 4 September 2022, which was the middle of the interval between the DSM acquisition dates (Fig. 12b).

It was assumed that the areas of maximum vertical surface displacement according to the DSM data corresponded to the areas of surface texture change (activity areas) according to the TAI data and that no changes occurred in the stable vertical surface areas. To test this assumption, the TAI map and the DSM difference map of the activity and stability areas were compared (Fig. 12), and also compared the high spatial resolution RGB images obtained by the company Sitemark from the UAV observations of 6 June and 6 September 2022 for the activity and stability areas (Figs 13 & 14). The contours of the zones of interest (Fig. 11) are marked with black lines in Figure 12

A1 (Fig. 13a, d) covered part of the pyrite concentrate slope. The dump surface was subject to frequent changes during the 2022 summer season (Fig. 12b), and in 2022 this area was one of the most heavily mined. The maximum TAI value here was 1. A reduction in surface elevation of up to 5.51 m occurred on the northern dump slope. Textural changes due to rockfall were also observed on the northern slope of the old open pit.

A2 (Fig. 13b, e) was close to industrial buildings and included three small waste dumps with some rock removed by September. The reduction in surface height was 6.71 m. Each of the waste dumps showed intense activity in individual pixel groups. Changes occurred on every date or on a majority of observation dates (Fig. 12b).

A proportion of the rock layer was also removed from the slope of the south waste dump in zone A3 (Fig. 13c, f), and the maximum height reduction was 2.82 m. The area of the activity zone was significantly larger than the area of elevation change, which was caused by changes in the texture of the scarp slope due to rock deposition. There were no changes in surface elevation in stability areas (Fig. 14).

In stability zones (Fig. 14), there were no changes in surface texture; the TAI values were equal to zero. Minor vertical displacements corresponded to changes in surface texture due to wind and water erosion of soil, as well as vehicle movements (S2 ; Fig. 14b). In S1 (Fig. 14a), vertical variations in surface height were *c.* 0.2 m in absolute value, and in S2 (Fig. 14b) they were *c.* 0.4 m, while in S3 (Fig. 14c) they were *c.* 0.1 m.

Dynamics of NDAI changes in the zones of interest

The dynamics of changes in the maximum NDAI were evaluated for May–September 2022 for each activity (Fig. 15a) and stability (Fig. 15c) zone, and box plots of the spatial maximum NDAI values (Fig. 15b, d) were generated for a time series of 43 observations.

The time series of spatial maximum NDAI values for each zone (Fig. 15a, c) show the maximum activity on each monitoring date relative to neighbouring dates. For example, in A1, the maximum activity was observed on 24 June 2022 and 11 August 2022. The dynamics of changes in the maximum NDAI in A2 at the beginning of the 2022 monitoring period approximated the dynamics in zone A1, with a maximum NDAI on 24 June 2022. For all zones, the maximum NDAI values exceeded the th_{NDAI} thresholds, generally indicating activity at at least one of the sites within each zone. In stability zones (Fig. 15c), the maximum NDAI values were predominantly below th_{NDAI}. In S1, the maximum NDAI was 0.21 on 11 August 2022, while in S2 the maximum NDAI was 0.29 on 30 July 2022. The maximum NDAI values within the stability zones, which were not significantly above the threshold, indicated small changes in the surface texture which may have been related to weather effects.

Box plots of the maximum NDAI for each zone (Fig. 15b, d) describe the frequency of surface changes over time (including those due to mining). The higher the median, the lower the interquartile range and the difference between the minimum and maximum, and the higher the frequency of surface change. For example, the median of the maximum spatial values of A3 was the highest (0.74) and the interquartile range was the lowest (0.11) (Fig. 15b), indicating a high intensity of surface change in the southern waste dump area compared to other zones. The largest interquartile range of maximum NDAIs was observed in A2 (0.24). During the observation period, relatively frequent activity was

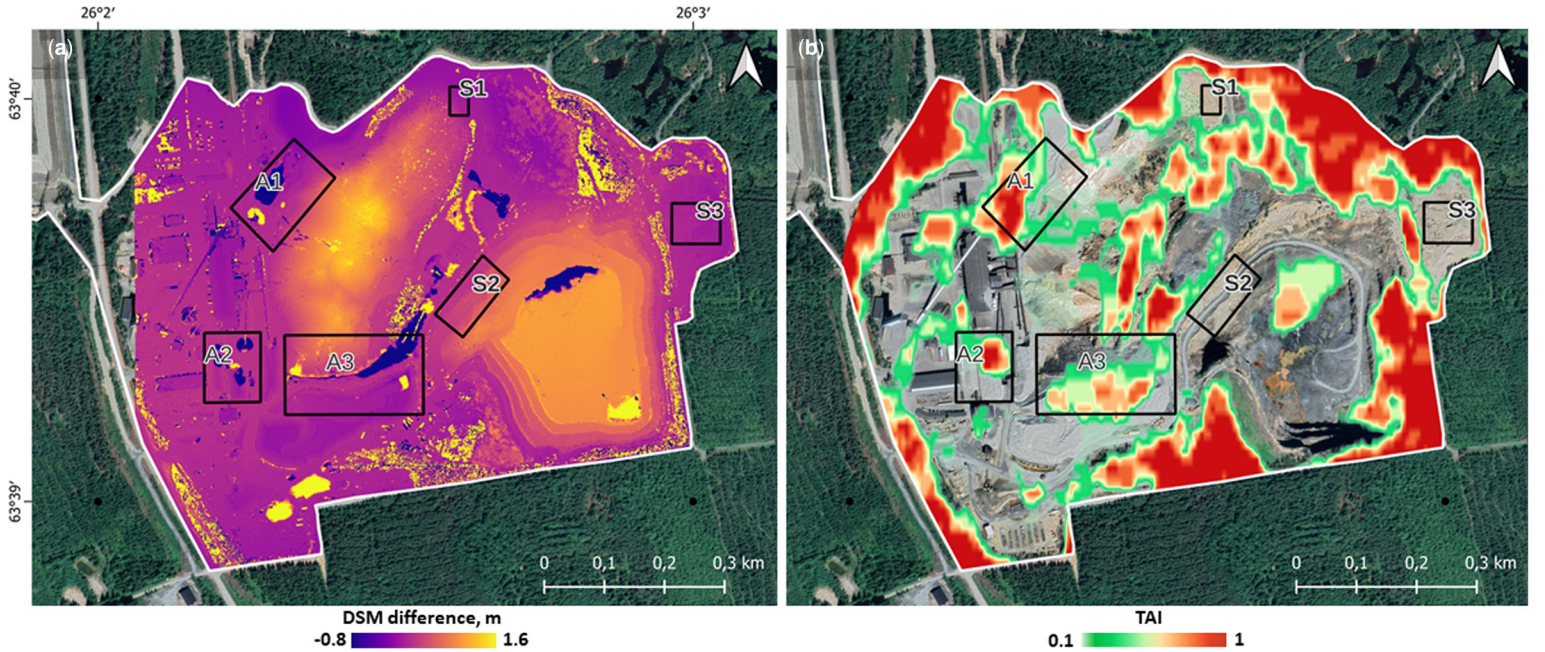

Fig. 12. Comparison of the digital surface model (DSM) difference map and temporal activity index (TAI) map. (**a**) DSM difference map between 6 June 2022 and 6 September 2022; (**b**) TAI map generated by normalized differential activity index (NDAI) data from 24 June 2022 to 4 September 2022. Source: basemap, Google Satellite (2024) Pyhäjärvi, available at https://www.google.com/maps (last accessed 18 March 2024).

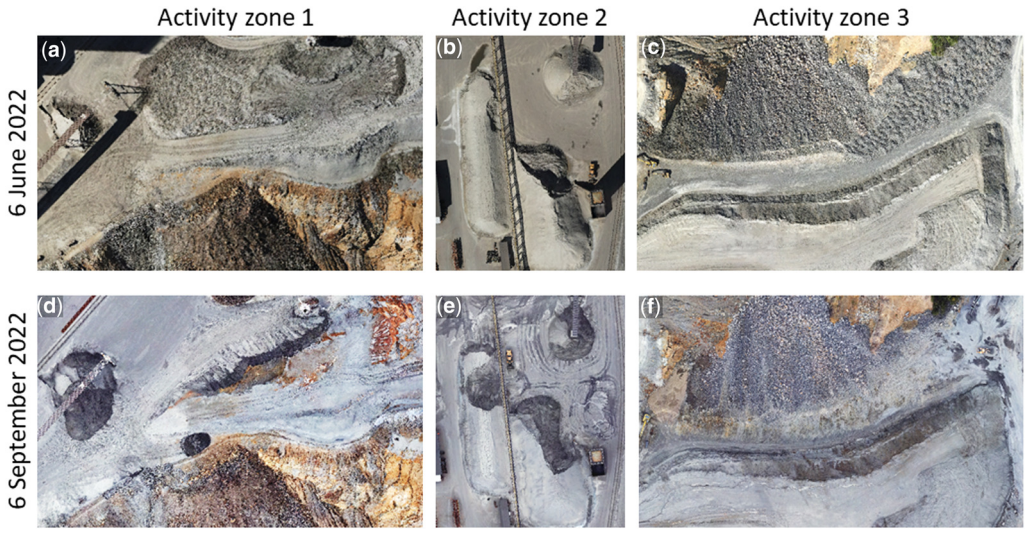

Fig. 13. Comparison of high spatial resolution RGB images of activity zones on 6 June 2022 and 6 September 2022: (**a**) activity zone 1, 6 June 2022; (**b**) activity zone 2, 6 June 2022; (**c**) activity zone 3, 6 June 2022; (**d**) activity zone 1, 6 September 2022; (**e**) activity zone 2, 6 September 2022; (**f**) activity zone 3, 6 September 2022.

observed in the northern dump area (A1). The median of the maximum NDAI values here was 0.63, and the interquartile range of the NDAI was 0.11. In stability zones (Fig. 15d), the median of spatially maximum NDAI values and the upper quartile did not exceed the threshold value th_{NDAI}, which generally indicated the absence of intensive activity at the sites.

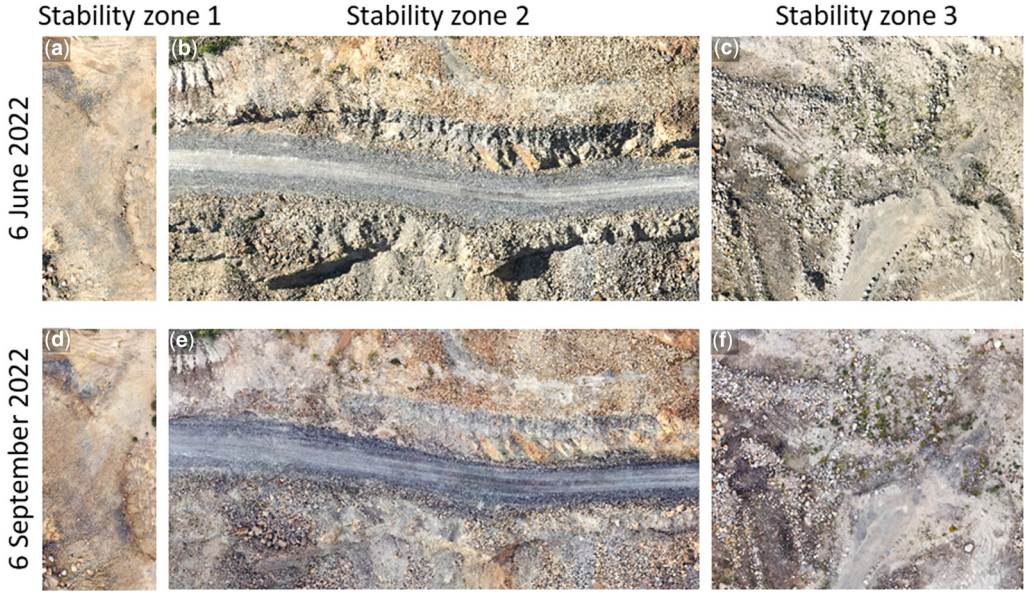

Fig. 14. Comparison of very high spatial resolution RGB images of stability zones for 6 June 2022 and 6 September 2022: (**a**) stability zone 1, 6 June 2022; (**b**) stability zone 2, 6 June 2022; (**c**) stability zone 3, 6 June 2022; (**d**) stability zone 1, 6 September 2022; (**e**) stability zone 2, 6 September 2022; (**f**) stability zone 3, 6 September 2022.

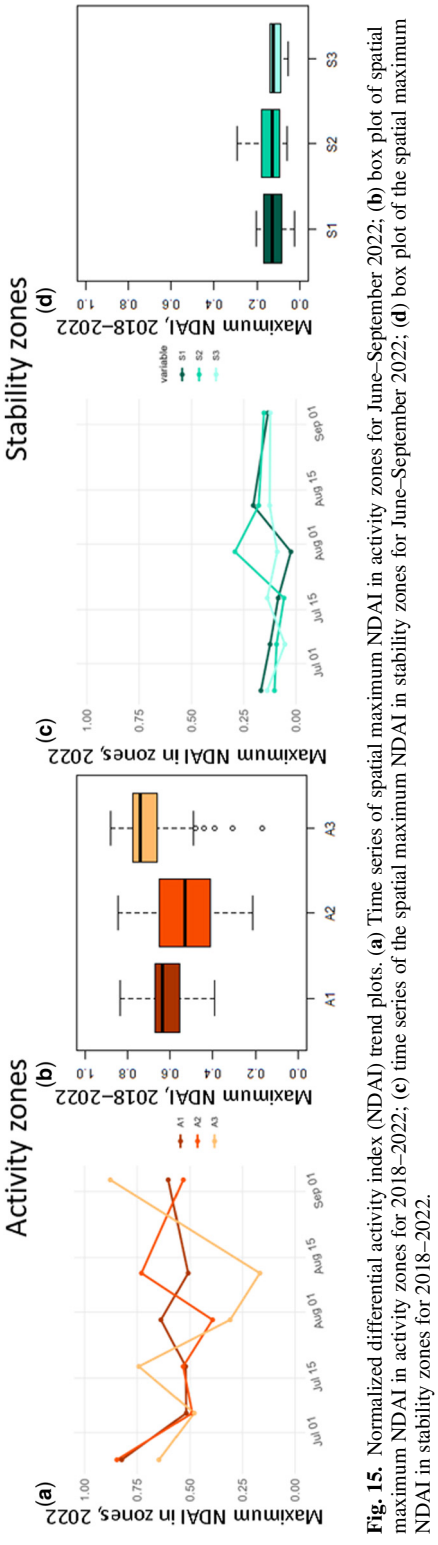

Fig. 15. Normalized differential activity index (NDAI) trend plots. (**a**) Time series of spatial maximum NDAI in activity zones for June–September 2022; (**b**) box plot of spatial maximum NDAI in activity zones for 2018–2022; (**c**) time series of the spatial maximum NDAI in stability zones for June–September 2022; (**d**) box plot of the spatial maximum NDAI in stability zones for 2018–2022.

Comparison of NDAI with coherence maps

The results of activity area detection based on coherence and NDAI maps were compared for two observation dates using thresholds found by the Otsu method. Figure 16 shows histograms of the coherence map (Fig. 16a), NDAI map (Fig. 16b), the functional relationship between coherence and the NDAI (Fig. 16c), activity maps generated using the threshold found by the Otsu method based on Sentinel-1 data on 24 June 2022 (Fig. 16d, e), and those based on the functional relationship between coherence and the NDAI (Fig. 16f).

The intermodal minimum of the NDAI histogram (Fig. 16b) was more pronounced and had a narrower range of values compared to the intermodal minimum of the coherence histogram (Fig. 16a), providing more clarity on the applicability of Otsu's method for finding the threshold.

The Otsu thresholds separating the activity and stability areas were $th_{NDAI} = 0.13$ and $th_{Coh} = 0.74$, respectively. The activity areas corresponded to the NDAI map pixels with values above th_{NDAI} (Fig. 16e) and coherence map pixels with values below th_{Coh} (Fig. 16d). The coherence-based activity map generated using the th_{Coh} threshold (Fig. 16d) contained a larger area of activity compared to the NDAI-based activity data (Fig. 16e). Considering the functional relationship between coherence and the NDAI, a value of $th_{NDAI} = 0.13$ corresponded to $th^{*}_{Coh} = 0.68$. In this case, the coincidence between the activity maps in Figure 16d, e was 99.7%.

Discussion

Comparison of coherence and NDAI maps

Coherence is a characteristic of invariability of the radar signal reflected from the Earth's surface on consecutive observation dates. The range of coherence values is fixed, making it possible to compare its absolute values on different dates. High coherence values are characteristic of stable areas. Unlike coherence, the NDAI is aimed at removing the decorrelation noise, identifying activity areas, and has high values in the case of surface changes in the interval between acquisitions. As the NDAI calculation is based on average coherence in stable pixels, the values of which are different for different dates, the range of NDAI values is not universal, and in some cases the NDAI may have negative values for stable areas.

As shown in Figure 8a, there was a non-linear (hyperbolic) dependence between the NDAI and coherence (Fig. 8a). This dependence was characteristic of all observation dates and allowed a mutually

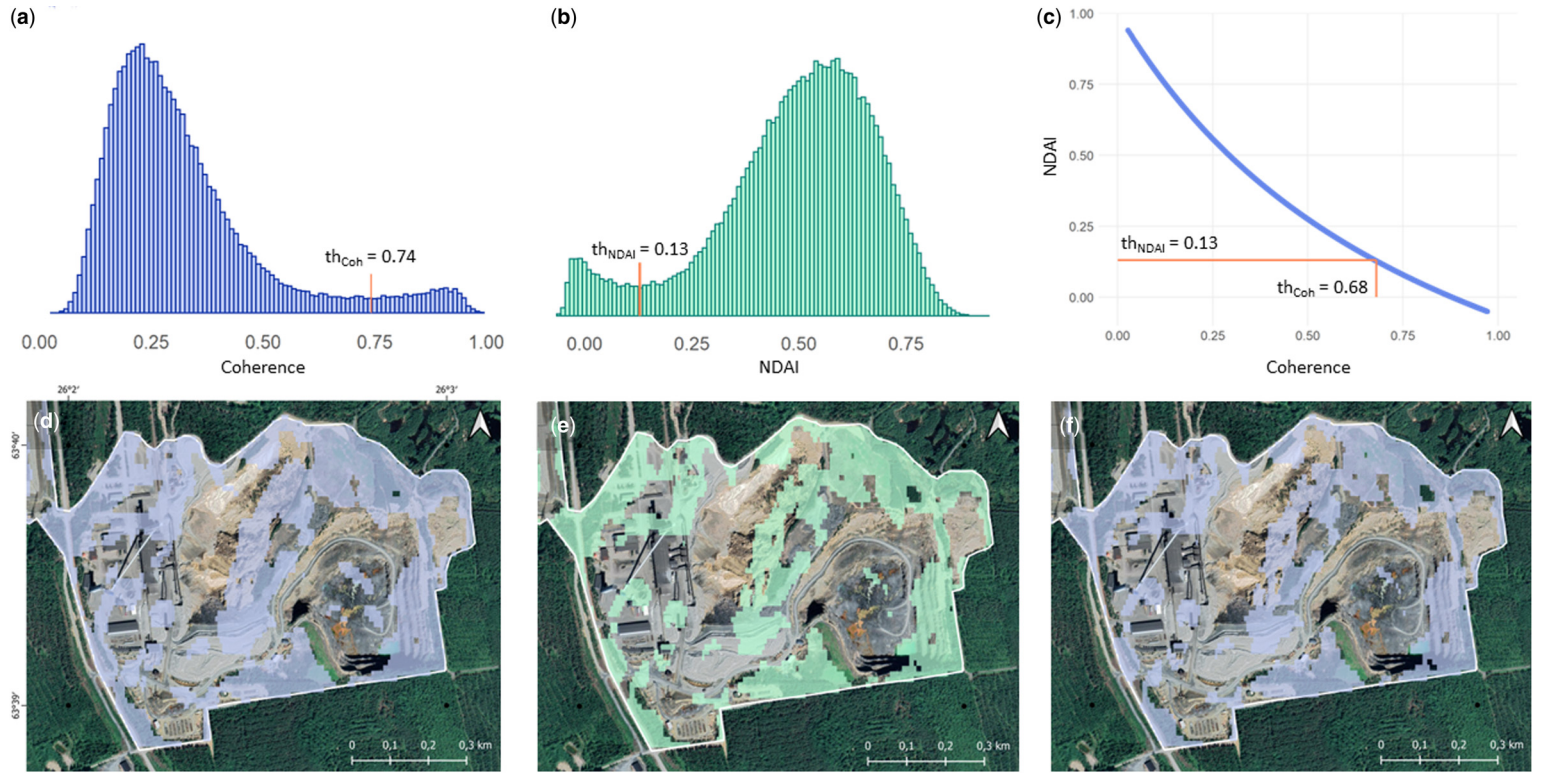

Fig. 16. Comparison of coherence and normalized differential activity index (NDAI) maps generated from Sentinel-1 data on 24 June 2022: (**a**) histogram of coherence with the labelled threshold value; (**b**) histogram of the NDAI with the labelled threshold value; (**c**) functional relationship between coherence and the NDAI; (**d**) activity map generated from coherence data based on the threshold value, found by the Otsu method; (**e**) activity map generated from NDAI data based on the threshold value found by the Otsu method; (**f**) activity map generated from coherence data based on the threshold value found by the functional relationship between coherence and the NDAI. Source: basemap, Google Satellite (2024) Pyhäjärvi, available at https://www.google.com/maps (last accessed 18 March 2024).

unambiguous correspondence between coherence and the NDAI to be established.

The study area was characterized by the presence of two modes in the histograms of coherence and the NDAI (Fig. 8b, d). The mode of low coherence values (high NDAI values) corresponded to activity areas and the second mode corresponded to stability areas. The presence of two modes made it possible to apply the Otsu method to find the threshold of coherence (th_{Coh}) and the NDAI (th_{NDAI}), separating the activity and stability regions. The hyperbolic dependence also described the relationship between thresholds th_{Coh} and th_{NDAI} at individual observation dates. The threshold for time-averaged NDAI maps, which differed from the thresholds on individual dates, was used in this paper.

The formation of an analytical model that provides the transition from coherence to the NDAI will make it possible to avoid the need for empirical calculations of the NDAI in order to reduce the influence of spatial and temporal decorrelation. The determination of such a dependence will be the subject of a separate study.

Influence of the perpendicular baseline

The results of activity area mapping are highly dependent on the Sentinel-1 acquisition parameters: flight direction, time interval between successive image acquisitions and the perpendicular baseline.

The section 'Calculation of NDAI' describes the influence of the perpendicular baseline value on the coherence variation. There was a decreasing trend in the linear regression of spatially averaged coherence values in stable pixels on the perpendicular baseline. It can be assumed that decorrelation can be removed by excluding from consideration image pairs for which the perpendicular baseline value is higher than some limit. However, the elimination of some of the images shortens the time series of observations and reduces the informativeness of the results. In addition, the significance and confidence interval of the correlation coefficient between the coherence values and perpendicular baseline changes with the number of images. When the number of images decreases, the significance decreases. In our case, the minimum number of Sentinel-1 image pairs significant for analysis was 40.

Comparison with displacement maps

Vertical and horizontal surface displacement velocities in the vicinity of the mine for the period 2019–2022 were calculated using Sentinel-1 SLC data (Fig. 17). An annual observation interval of 23 April–26 October was used. Observations were made during the snowless period. Ascending and descending orbit data are required to produce surface displacement velocity maps. The 160th ascending and the 153rd descending orbits were selected and the surveys for these orbits were carried out on the same dates. From 2019 to 2021, surveys were performed at 6-day intervals and in 2022 at 12-day intervals. Time series and displacement maps were generated from the unwrapped interferograms using the MintPy application. The resulting displacement velocity maps were represented by raster grids at a spatial resolution of 40 m.

For all observation dates, the minimum and maximum vertical displacement velocities were −0.061 m yr^{-1} (2020) and 0.046 m yr^{-1} (2022). The minimum and maximum horizontal displacement

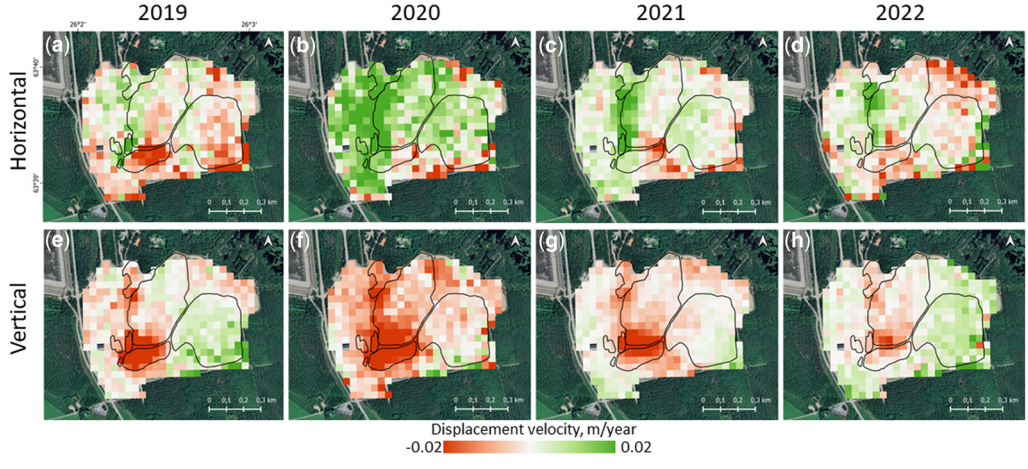

Fig. 17. Horizontal and vertical displacement velocity maps for 2019–2022. Source: basemap, Google Satellite (2024) Pyhäjärvi, available at https://www.google.com/maps (last accessed 18 March 2024).

velocities were -0.104 m yr^{-1} (2019) and 0.057 m yr^{-1} (2020). The whole range of vertical and horizontal displacement velocities was divided into equal intervals from -0.02 to 0.02 m yr^{-1}. This interval covered more than 90% of the displacements. The 'equal intervals' classification scheme was chosen to compare results between years (Fig. 17). Individual pixels with velocity values outside the specified range were assigned to boundary classes. Note that the red colour in Figure 17 (negative velocities) indicates movement away from the satellite, while the green colour (positive velocities) indicates movement towards the satellite (Shi *et al.* 2020).

The maximum absolute vertical displacement velocities were observed near the northern slope of the old open pit for all years of monitoring. High TAI values were also observed (Fig. 10g–j), which generally characterizes this area as unstable and subject to change. Maximum positive horizontal displacement velocities were mainly observed in the western part of the mine site near the old open-pit slope, in the northern waste dump area and in the vicinity of the administrative buildings, which was most noticeable in 2020.

Limitations and opportunities

The proposed approach has some limitations that affect the accuracy of the result and are caused by the influence of weather conditions, surface characteristics, the inclined nature of satellite images and their spatial resolution. Heavy precipitation, especially snow cover, increases decorrelation and requires the exclusion of some images from consideration, reducing the time series and lowering the informativeness of the result.

Water surfaces and areas of vegetation cover, such as tailings ponds covered with a water mixture of industrial waste, as well as forests and meadows in the vicinity of the mine, are also low coherent. They have to be identified in advance and excluded from subsequent analyses. Increasing the perpendicular baseline also reduces coherence.

Due to the inclined survey, radar shadows are present on uneven surfaces (slopes of open pits, dumps). Shadow areas are characterized by low coherence and can be misinterpreted as areas of activity.

The spatial resolution of coherence, NDAI and TAI maps is 20 m. This resolution does not exclude the presence of mixed pixels and reduces the sensitivity of the method to local small surface changes. In addition, the coherence and NDAI maps detect changes in surface texture but do not reliably detect elevation variations. Such variations are most accurately tracked by differences in DSM maps generated from ultra-high spatial resolution UAV images.

Promising directions for the development of the presented approach to improve the accuracy of activity and stability area mapping are the analysis of SAR data acquired simultaneously from ascending and descending orbits, and the generation of complex indicators that take into account horizontal and vertical surface changes. The calculation of such indicators is the subject of future research.

Conclusions

For the Pyhäsalmi Mine area, surface mining activity and stability areas were mapped using Sentinel-1 coherence time series for the observation period from 2018 to 2022. A method for calculating the TAI based on the NDAI was proposed. This method was found to be robust to spatial and temporal decorrelation of the radar signal. The NDAI thresholds separating activity and stability areas were selected using the Otsu method for time-averaged NDAI maps. For several activity and stability zones, the dynamics of changes in time of the maximum activity of the NDAI time series for the summer season of 2022 were estimated.

The results obtained made it possible to identify the areas of open-pit production processes, and the formation and removal of waste dumps, and to estimate the intensity of these processes based on TAI values in each season of observation. Maximum TAI values (the highest activity) were observed mostly in the backfill open pit and near its eastern edge, in the waste dump area near industrial buildings and facilities, on the slopes of the pyrite dump in the northern part of study area, and on the southern slope of the old open pit. The most intense changes were observed in 2020 and 2021. The activity zone at the bottom of the backfill open pit moved from its southwestern to its northeastern part during the observation period. The continuous changes on the surface of the southern and eastern slopes of the old open pit were mainly related to work near the open-pit boundaries and to rock crumbling. The TAI maps also showed intense working dynamics on the waste dump surface due to continuous changes in the slope shape and waste dump height. Other areas of the mine site, including the northern part of the backfill open pit, the northern and eastern slopes of the old open pit, and the open area in the western part of the mine site, are mostly unaffected by changes (TAI values close to zero), and small TAI values in some areas of stability were caused by weathering (wind and rain erosion), sparse vegetation or radar shadows. Validation of the results on DSM difference maps based on the 2022 UAV observations showed that the selected areas of activity corresponded to the vertical displacement zones and confirmed the validity of the results.

The NDAI maps generated from the coherence maps allowed removal of decorrelation unrelated to mining operations but required additional computation and increased data processing time. Establishing a functional dependence for the direct transition from coherence to the NDAI will significantly reduce the computational cost. The search for such a dependence will be a topic for future research.

Acknowledgements The authors gratefully acknowledge Maria Hänninen, Environmental Manager at Pyhäsalmi Mine Oy for specification locations for measurements and study planning, and the OPT/NET BV company (opt-net.eu) and GOLDEN-AI platform for supplying Sentinel-1 data. The authors would like to thank the European Commission, the European Space Agency and the Copernicus Programme for providing Sentinel-1 data.

Competing interests The authors declare that they have no known competing financial interests or personal relationships that could have appeared to influence the work reported in this paper.

Author contributions **OK**: conceptualization (equal), methodology (equal), validation (equal), visualization (equal), writing – original draft (equal), writing – review & editing (equal); **DK**: conceptualization (equal), methodology (equal), validation (equal), visualization (equal), writing – original draft (equal), writing – review & editing (equal); **KS**: conceptualization (equal), methodology (equal), validation (equal), visualization (equal), writing – original draft (equal), writing – review & editing (equal).

Funding This work was funded by the European Union's Horizon 2020 research and innovation programme under grant agreement no. 869398 'Earth observation and Earth GNSS data acquisition and processing platform for safe, sustainable and cost-efficient mining operations' (Goldeneye).

Data availability All data generated or analysed during this study are included in this published article (and, if present, its supplementary information files).

References

Abrams, M., Crippen, R. and Fujisada, H. 2020. ASTER global digital elevation model (GDEM) and ASTER global water body dataset (ASTWBD). *Remote Sensing*, **12**, 1156, https://doi.org/10.3390/rs12071156

Agamennoni, G., Nieto, J. and Nebot, E. 2009. Mining GPS data for extracting significant places. IEEE International Conference on Robotics and Automation Conference Proceedings, 12–17 May 2009, Kobe, Japan, 855–862, https://doi.org/10.1109/ROBOT.2009.5152475

AIRBUS. 2020. *Copernicus DEM: Copernicus Digital Elevation Model Product Handbook*. **Report AO/1-9422/18/IL G**.

Amani, M., Poncos, V., Brisco, B., Foroughnia, F., DeLancey, E.R. and Ranjbar, S. 2021. InSAR coherence analysis for wetlands in Alberta, Canada using time-series Sentinel-1 data. *Remote Sensing*, **13**, 3315, https://doi.org/10.3390/rs13163315

Borlaf-Mena, I., Badea, O. and Tanase, M.A. 2021. Assessing the utility of Sentinel-1 coherence time series for temperate and tropical forest mapping. *Remote Sensing*, **13**, 4814, https://doi.org/10.3390/rs13234814

Camalan, S., Cui, K. *et al*. 2022. Change detection of Amazonian alluvial gold mining using deep learning and Sentinel-2 imagery. *Remote Sensing*, **14**, 1746, https://doi.org/10.3390/rs14071746

Chatterjee, R.S., Lakhera, R.C. and Dadhwal, V.K. 2010. InSAR coherence and phase information for mapping environmental indicators of opencast coal mining: a case study in Jharia Coalfield, Jharkhand, India. *Canadian Journal of Remote Sensing*, **36**, 361–373, https://doi.org/10.5589/m10-047

COP-DEM. 2019. European digital elevation model, https://spacedata.copernicus.eu/collections/copernicus-digital-elevation-model

Devanthéry, N., Crosetto, M., Cuevas-González, M., Monserrat, O., Barra, A. and Crippa, B. 2016. Deformation monitoring using persistent scatterer interferometry and Sentinel-1 SAR data. *Procedia Computer Science*, **100**, 1121–1126, https://doi.org/10.1016/j.procs.2016.09.263

Escayo, J., Marzan, I. *et al*. 2022. Radar interferometry as a monitoring tool for an active mining area using Sentinel-1 C-Band Data, case study of Riotinto Mine. *Remote Sensing*, **14**, 3061, https://doi.org/10.3390/rs14133061

Fernández-Lozano, J., González-Díez, A. *et al*. 2018. New perspectives for UAV-based modelling the roman gold mining infrastructure in NW Spain. *Minerals*, **8**, 518, https://doi.org/10.3390/min8110518

Foumelis, M., Blasco, J.M.D. *et al*. 2018. ESA SNAP-StaMPS integrated processing for Sentinel-1 persistent scatterer interferometry. IGARSS 2018-2018 IEEE International Geoscience and Remote Sensing Symposium, 22–27 July 2018, Valencia, Spain, 1364–1367, https://doi.org/10.1109/IGARSS.2018.8519545

Funning, G.J. and Garcia, A. 2019. A systematic study of earthquake detectability using Sentinel-1 Interferometric Wide-Swath data. *Geophysical Journal International*, **216**, 332–349, https://doi.org/10.1093/gji/ggy426

Gama, F.F., Mura, J.C., Paradella, W.R. and Oliveira, C.G. 2020. Deformations prior to the Brumadinho dam collapse revealed by sentinel-1 InSAR data using SBAS and PSI techniques. *Remote Sensing*, **12**, 3664, https://doi.org/10.3390/rs12213664

Havisto, J., Matselyukh, T. *et al*. 2021. Golden AI data acquisition and processing platform for safe, sustainable and cost-efficient mining operations. 2021 IEEE International Geoscience and Remote Sensing Symposium IGARSS, 11–16 July 2021, Brussels, Belgium, 5775–5778, https://doi.org/10.1109/IGARSS47720.2021.9554181

Hijmans, R.J. 2022. Terra: Spatial Data Analysis. R Package Version 1.5-21, https://CRAN.R-project.org/package=terra

Hu, J., Ge, Q., Liu, J., Yang, W., Du, Z. and He, L. 2021. Constructing adaptive deformation models for estimating DEM error in SBAS-InSAR based on hypothesis testing. *Remote Sensing*, **13**, 2006, https://doi.org/10.3390/rs13102006

Jacob, A.W., Vicente-Guijalba, F. *et al*. 2020. Sentinel-1 InSAR coherence for land cover mapping: a comparison of multiple feature-based classifiers. *IEEE Journal of Selected Topics in Applied Earth Observations and Remote Sensing*, **13**, 535–552, https://doi.org/10.1109/JSTARS.2019.2958847

Kavats, O., Khramov, D., Sergieieva, K. and Vasyliev, V. 2020. Monitoring of sugarcane harvest in Brazil based on optical and SAR data. *Remote Sensing*, **12**, 4080, https://doi.org/10.3390/rs12244080

Kavats, O., Khramov, D. and Sergieieva, K. 2022. Surface water mapping from SAR images using optimal threshold selection method and reference water mask. *Water*, **14**, 4030, https://doi.org/10.3390/w14244030

Kellndorfer, J., Cartus, O. *et al*. 2022. Global seasonal Sentinel-1 interferometric coherence and backscatter data set. *Scientific Data*, **9**, 1–16, https://doi.org/10.1038/s41597-022-01189-6

Kotavaara, O., Domenech, G. *et al*. 2023. Interferometric Synthetic Aperture Radar (InSAR)-based measurements of displacements due to geomorphologic changes in northern mining environments – testing and validating InSAR in open pit and tailings of Pyhäsalmi Mine, Finland. Copernicus Meetings. EGU General Assembly, 24–28 April 2023, Vienna, Austria, https://doi.org/10.5194/egusphere-egu23-6208

Lee, H. and Liu, J.G. 2001. Analysis of topographic decorrelation in SAR interferometry using ratio coherence imagery. *IEEE Transactions on Geoscience and Remote Sensing*, **39**, 223–232, https://doi.org/10.1109/36.905230

Lu, C.H., Ni, C.F., Chang, C.P., Yen, J.Y. and Chuang, R.Y. 2018. Coherence difference analysis of sentinel-1 SAR interferogram to identify earthquake-induced disasters in urban areas. *Remote Sensing*, **10**, 1318, https://doi.org/10.3390/rs10081318

Lu, Y., Yang, C. and Jiang, Q. 2021. Evaluation of the performance of time-series Sentinel-1 data for discriminating rock units. *Remote Sensing*, **13**, 4824, https://doi.org/10.3390/rs13234824

Mäkinen, J. and Lerssi, J. 2007. Characteristics and seasonal variation of sediments in Lake Junttiselkä, Pyhäsalmi, Finland. *Mine Water and the Environment*, **26**, 217–228, https://doi.org/10.1007/s10230-007-0015-3

Manzoni, M., Molinari, M.E. and Monti-Guarnieri, A. 2021. Multitemporal InSAR coherence analysis and methods for sand mitigation. *Remote Sensing*, **13**, 1362, https://doi.org/10.3390/rs13071362

Moon, J. and Lee, H. 2021. Analysis of activity in an open-pit mine by using InSAR coherence-based normalized difference activity index. *Remote Sensing*, **13**, 1861, https://doi.org/10.3390/rs13091861

Nam, B.X., Van Anh, T., Bui, L.K., Long, N.Q., Le Thu Ha, T. and Goyal, R. 2021. Mining-induced land subsidence detection by persistent scatterer InSAR and sentinel-1: application to Phugiao Quarries, Vietnam. *In*: Tien Bui, D., Tran, H.T. and Bui, X.-N. (eds) *Proceedings of the International Conference on Innovations for Sustainable and Responsible Mining: ISRM 2020 – Volume 2*. Springer, Cham, 18–38, https://doi.org/10.1007/978-3-030-60269-7_2

Olen, S. and Bookhagen, B. 2018. Mapping damage-affected areas after natural hazard events using sentinel-1 coherence time series. *Remote Sensing*, **10**, 1272, https://doi.org/10.3390/rs10081272

Otsu, N. 1979. A threshold selection method from gray-level histograms. *IEEE Transactions on Systems, Man, and Cybernetics*, **9**, 62–66, https://doi.org/10.1109/TSMC.1979.4310076

Parwata, I.N.S., Nakashima, S., Shimizu, N. and Osawa, T. 2020. Effect of digital elevation models on monitoring slope displacements in open-pit mine by differential interferometry synthetic aperture radar. *Journal of Rock Mechanics and Geotechnical Engineering*, **12**, 1001–1013, https://doi.org/10.1016/j.jrmge.2020.01.003

Potin, P., Colin, O. *et al*. 2022. Status and evolution of the Sentinel-1 mission. IGARSS 2022–2022 IEEE International Geoscience and Remote Sensing Symposium, 17–22 July 2022, Kuala Lumpur, Malaysia, 4707–4710, https://doi.org/10.1109/IGARSS46834.2022.9884753

R Core Team. 2020. *The R Project for Statistical Computing*. R Foundation for Statistical Computing, Vienna, Austria, https://www.r-project.org

Ren, H., Zhao, Y., Xiao, W. and Hu, Z. 2019. A review of UAV monitoring in mining areas: current status and future perspectives. *International Journal of Coal Science & Technology*, **6**, 320–333, https://doi.org/10.1007/s40789-019-00264-5

RStudio Team. 2022. *RStudio: Integrated Development Environment for R*. RStudio, PBC, Boston, MA, USA, https://posit.co/products/open-source/rstudio

Santillan, J.R. and Makinano-Santillan, M. 2016. Vertical accuracy assessment of 30-M resolution ALOS, ASTER, and SRTM global DEMS over Northeastern Mindanao, Philippines. *The International Archives of the Photogrammetry, Remote Sensing and Spatial Information Sciences*, **41**, 149–156, https://doi.org/10.5194/isprsarchives-XLI-B4-149-2016

Sergieieva, K., Kavats, O. and Khramov, D. 2023. Monitoring active mining areas in operation using Sentinel-1 coherence time series. Copernicus Meetings. EGU General Assembly, 24–28 April 2023, Vienna, Austria, https://doi.org/10.5194/egusphere-egu23-5181

Shi, X., Zhang, L., Zhong, Y., Zhang, L. and Liao, M. 2020. Detection and characterization of active slope deformations with Sentinel-1 InSAR analyses in the southwest area of Shanxi, China. *Remote Sensing*, **12**, 392, https://doi.org/10.3390/rs12030392

Siikanen, S., Savolainen, M., Karinen, A., Puputti, J., Kauppinen, T., Uusitalo, S. and Paavola, M. 2022. Drone-based near-infrared multispectral and hyperspectral imaging in monitoring structural changes in mine tailing ponds. *Thermosense: Thermal Infrared Applications XLIV*, **12 109**, 58–64, https://doi.org/10.1117/12.2618294

Takaku, J., Tadono, T., Doutsu, M., Ohgushi, F. and Kai, H. 2020. Updates of 'AW3D30'ALOS global digital surface model with other open access datasets. *The International Archives of the Photogrammetry, Remote*

Sensing and Spatial Information Sciences, **43**, 183–189, https://doi.org/10.5194/isprs-archives-XLIII-B4-2020-183-2020

Tang, W., Motagh, M. and Zhan, W. 2020. Monitoring active open-pit mine stability in the Rhenish coalfields of Germany using a coherence-based SBAS method. *International Journal of Applied Earth Observation and Geoinformation*, **93**, 102 217, https://doi.org/10.1016/j.jag.2020.102217

Villarroya-Carpio, A., Lopez-Sanchez, J.M. and Engdahl, M.E. 2022. Sentinel-1 interferometric coherence as a vegetation index for agriculture. *Remote Sensing of Environment*, **280**, 113 208, https://doi.org/10.1016/j.rse.2022.113208

Wang, K., Xu, X. and Fialko, Y. 2017. Improving burst alignment in TOPS interferometry with bivariate enhanced spectral diversity. *IEEE Geoscience and Remote Sensing Letters*, **14**, 2423–2427, https://doi.org/10.1109/LGRS.2017.2767575

Wang, S., Lu, X., Chen, Z., Zhang, G., Ma, T., Jia, P. and Li, B. 2020. Evaluating the feasibility of illegal open-pit mining identification using InSAR coherence. *Remote Sensing*, **12**, 367, https://doi.org/10.3390/rs12030367

Wang, L., Yang, L., Wang, W., Chen, B. and Sun, X. 2021. Monitoring mining activities using Sentinel-1A InSAR coherence in open-pit coal mines. *Remote Sensing*, **13**, 4485, https://doi.org/10.3390/rs13214485

Wang, S., Bai, Z., Lv, Y. and Zhou, W. 2022. Monitoring extractive activity-induced surface subsidence in highland and alpine opencast coal mining areas with multi-source data. *Remote Sensing*, **14**, 3442, https://doi.org/10.3390/rs14143442

Washaya, P., Balz, T. and Mohamadi, B. 2018. Coherence change-detection with Sentinel-1 for natural and anthropogenic disaster monitoring in urban areas. *Remote Sensing*, **10**, 1026, https://doi.org/10.3390/rs10071026

Wei, L., Feng, Q. *et al*. 2020. Precise topographic model assisted slope displacement retrieval from small baseline subsets results: case study over a high and steep mining slope. *Sensors*, **20**, 6674, https://doi.org/10.3390/s20226674

Wu, Q., Song, C., Liu, K. and Ke, L. 2020. Integration of TanDEM-x and SRTM DEMs and spectral imagery to improve the large-scale detection of opencast mining areas. *Remote Sensing*, **12**, 1451, https://doi.org/10.3390/rs12091451

Yang, L., Meng, X. and Zhang, X. 2011. SRTM DEM and its application advances. *International Journal of Remote Sensing*, **32**, 3875–3896, https://doi.org/10.1080/01431161003786016

Zhang, J. 2021. InSAR collaborative monitoring mode and multi-mode computing services for geohazards identification in open-pit mining area. *The International Archives of the Photogrammetry, Remote Sensing and Spatial Information Sciences*, **43**, 241–247, https://doi.org/10.5194/isprs-archives-XLIII-B1-2021-241-2021

Zhang, L., Ge, D., Guo, X., Liu, B., Li, M. and Wang, Y. 2020. InSAR monitoring surface deformation induced by underground mining using Sentinel-1 images. *Proceedings of the International Association of Hydrological Sciences*, **382**, 237–240, https://doi.org/10.5194/piahs-382-237-2020